Chemical Physics 597 (2025) 112778

Contents lists available at ScienceDirect

Chemical Physics

journal homepage: www.elsevier.com/locate/chemphys

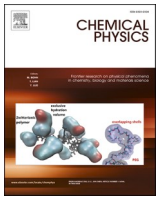

Intrinsic thermoelectric performance enhancement of $Bi_2Al_4S_8$ via carrier concentration and chemical potential engineering

T. Ghellab [a,b], A. Zikem [a,c], H. Baaziz [a,b,*], Z. Charifi [a,b]

[a] Laboratory of Physics and Chemistry of Materials, University of M'sila, Algeria
[b] Department of Physics, Faculty of Science, University of M'sila, 28000, M'sila, Algeria
[c] National School of Built and Ground Works Engineering, B.P. 32, Kouba, Algiers, Algeria

ARTICLE INFO

Keywords:
Optoelectronic properties
Mechanical stability
Seebeck coefficient
Figure of merit (ZT)
Photovoltaic applications
Energy conversion

ABSTRACT

This study presents a comprehensive computational analysis of the structural, electronic, optical, elastic, and thermoelectric properties of $Bi_2Al_4S_8$, a metastable tetragonal compound with promising applications in optoelectronics, photovoltaics, and thermoelectric energy conversion. Density functional theory (DFT) calculations, employing both the LDA and the mBJ potential, were used to determine the optimized structural parameters, electronic band structure, density of states, optical response, elastic constants, and thermoelectric transport coefficients. $Bi_2Al_4S_8$ exhibits an indirect bandgap of 2.589 eV (LDA) and 3.234 eV (mBJ), making it suitable for photovoltaic applications. Optical property analyses reveal strong visible-light absorption, a static dielectric constant of 6, and a refractive index of 2.4, indicating its potential for efficient light-harvesting devices. The mechanical stability of $Bi_2Al_4S_8$ is confirmed by its elastic constants, with a bulk modulus of 70.1896 GPa and low anisotropy.

Furthermore, thermoelectric performance evaluations indicate that $Bi_2Al_4S_8$ exhibits an improved thermoelectric figure of merit (ZT), increasing from 0.6412 at $n_o = 65.7670 \times 10^{19}$ cm^{-3} to 0.9524 at $n = -29.26049 \times 10^{21}$ cm^{-3} or when the chemical potential shifts from 0.20424 eV to 0.3117 eV. This enhancement is achieved through intrinsic tuning of the carrier concentration and chemical potential, without the introduction of extrinsic dopants. These findings highlight $Bi_2Al_4S_8$ as a non-toxic, mechanically robust, and multifunctional material, encouraging further experimental validation and advancing its prospects for integration into next-generation renewable energy and thermoelectric technologies.

1. Introduction

Over the past two decades, quasi-binary systems incorporating sesqui-chalcogenides (M_2X_3), where M denotes group 13 or 15 elements and X represents chalcogens, have attracted substantial attention due to their remarkable physical properties. These materials exhibit high piezoelectricity, ferroelectricity, and ferroelasticity, making them indispensable for various advanced technological applications [1–4]. Among these properties, thermoelectric performance has emerged as a particularly promising area of research, driven by the growing demand for efficient energy conversion technologies.

Thermoelectric materials, which can directly convert heat into electricity, are critical for waste heat recovery, sustainable energy generation, and advanced cooling systems. The efficiency of thermoelectric materials is quantified by the dimensionless figure of merit $ZT = \frac{\sigma S^2 T}{(k_T)}$, where S is the Seebeck coefficient, σ is the electrical conductivity, T is the absolute temperature, and k_T is the total thermal conductivity (comprising electronic and lattice contributions). Achieving a high ZT requires a delicate balance between these parameters, often pursued through strategies such as band engineering, nanostructuring, and defect engineering.

For instance, Bi_2Te_3-based materials are well-known for their excellent thermoelectric performance at near-room temperatures. In particular, $Bi_{2-x}Sb_xTe_3$ samples exhibit high ZT values: 1.04 at 440 K for MW-Bi_2Te_3 and 0.76 at 523 K for MW-$Bi_{0.5}Sb_{1.5}Te_3$, while MA-Bi_2Te_3 and MA-$Bi_{0.5}Sb_{1.5}Te_3$ samples achieved maximum ZT values of 0.74 at 460 K and 0.27 at 300 K, respectively, as n- and p-type materials [5].

Additionally, $PbTe$ and other lead chalcogenide-based compounds (e.g., $PbSe$, PbS) are prominent thermoelectric materials, particularly effective in the mid-temperature range (600–800 K). Single-phase $PbTe$

* Corresponding author at: Laboratory of Physics and Chemistry of Materials, University of M'sila, Algeria.
E-mail address: hakimbaaziz@univ-msila.dz (H. Baaziz).

https://doi.org/10.1016/j.chemphys.2025.112778
Received 14 March 2025; Received in revised form 30 April 2025; Accepted 15 May 2025
Available online 29 May 2025

exhibits a ZT value of approximately 0.8 at room temperature, and through optimization techniques such as doping and nanostructuring, ZT values as high as 1.4 have been achieved [6].

In this context, $Bi_2Al_4S_8$ emerges as a promising and relatively unexplored sesqui-chalcogenide candidate for thermoelectric applications. Crystallizing in a complex tetragonal structure conducive to low lattice thermal conductivity, this compound incorporates bismuth—a heavy element known to enhance the Seebeck coefficient via strong carrier scattering and increased density of states near the *Fermi* level. The synergy between bismuth and aluminum provides a balance between high electronic mobility and mechanical stability. Furthermore, its composition of non-toxic and earth-abundant elements supports its potential for sustainable energy technologies. However, to date, no studies have comprehensively examined its thermoelectric performance.

The versatility of sesqui-chalcogenide systems arises from the wide range of behaviors they exhibit, which are strongly influenced by their elemental composition. Depending on the specific combination of constituent elements, these compounds can form limited solid solutions, complete solid solutions, or even complex ternary and quaternary phases. Notably, materials such as $BiInS_3$, $Bi_2In_4S_9$, and $Bi_2Ga_4Se_8$ [7] have been shown to exhibit a rich variety of physical properties, including distinctive structural motifs and functional attributes, making them attractive for diverse applications in optoelectronics and energy conversion. Their thermoelectric efficiency is influenced by factors such as electronic band structure, lattice thermal conductivity, and carrier mobility. For instance, the presence of heavy elements like bismuth often leads to strong spin–orbit coupling, which can enhance the Seebeck coefficient by increasing the density of states near the Fermi level. Additionally, the complex crystal structures of these materials, characterized by low-symmetry arrangements and anharmonic lattice vibrations, effectively reduce lattice thermal conductivity—a critical factor in achieving high ZT values. This structural and compositional diversity provides a fertile ground for discovering novel materials with potential applications in optoelectronics, thermoelectrics, and photovoltaics.

Particularly compelling is the use of abundant and non-toxic materials, such as bismuth-based compounds, which offer opportunities for enhancing device efficiency and sustainability. Bismuth-based materials have already demonstrated promise in optoelectronic devices, including photodetectors [8–10], and are being actively investigated for solar-driven hydrogen production, pollutant degradation [11–13], and clean-powered technologies such as batteries and thermoelectric generators [14–17]. Their thermoelectric potential is especially noteworthy due to the intrinsically low thermal conductivity associated with the heavy atomic mass of bismuth and the resulting phonon scattering. Furthermore, the stereochemically active lone pair electrons of Bi^{3+} ions contribute to asymmetric bonding and complex crystal structures, further suppressing heat transport while maintaining favorable electronic properties. These features make bismuth-based sesqui-chalcogenides attractive candidates for next-generation thermoelectric materials, with potential utility extending to therapeutic applications such as photothermal therapy and bioimaging [18–20].

Within this family, the $Bi_2Al_4S_8$ compound represents a promising yet underexplored material. In contrast to its counterparts, such as $Bi_2Ga_4Se_8$ and $Bi_2In_4S_9$, which have been extensively studied for their intriguing properties [4,21,22], $Bi_2Al_4S_8$ has received comparatively limited attention. This research gap is particularly significant given the potential advantages of incorporating aluminum—a lighter and more abundant element—into the $Bi_2Al_4S_8$ structure. The substitution of heavier elements with aluminum may alter the electronic structure and influence thermal transport properties through modified phonon scattering mechanisms. Such compositional variation offers the possibility of enhancing the power factor ($S^2\sigma$) while simultaneously reducing the lattice thermal conductivity.

Previous studies [23] have reported the synthesis and preliminary characterization of $Bi_2Al_4S_8$ and related compounds, including $Bi_2Al_4Se_8$, $Bi_2Ga_4S_8$, and mixed systems such as $Bi_2Al_2Ga_2S_8$. However, comprehensive insights into the structural, electronic, optical, and elastic properties of $Bi_2Al_4S_8$ remain scarce. Understanding these properties is essential for evaluating the material's potential in practical applications, particularly in thermoelectrics, where optimizing the interplay between electronic and thermal transport properties is crucial for achieving high ZT values. The likely layered or low-symmetry crystal structure of $Bi_2Al_4S_8$ may naturally facilitate phonon scattering while retaining sufficient electrical conductivity, thereby enhancing its thermoelectric efficiency. Additionally, the possibility of tuning its electronic properties through defect engineering or doping further underscores the material's potential.

This study addresses a key knowledge gap by performing a comprehensive first-principles investigation of $Bi_2Al_4S_8$. Using density functional theory (DFT), we analyze its structural stability, electronic band structure, optical response, and elastic properties, with a focus on thermoelectric potential. Specifically, we explore how intrinsic tuning—through variations in carrier concentration and chemical potential—affects transport parameters such as the Seebeck coefficient and figure of merit (ZT), without introducing explicit dopants or defects. Thermoelectric performance is assessed by calculating the Seebeck coefficient, electrical and thermal conductivities across a range of temperatures. These results provide valuable insights into $Bi_2Al_4S_8$ and contribute to the broader field of sesqui-chalcogenides, supporting future experimental validations and applications in sustainable energy technologies.

2. Computational details

Density Functional Theory (DFT) is a widely used computational approach for investigating the structural, electronic, and optical properties of crystalline materials. In this study, the ground-state structural properties of the compounds were determined by relaxing and optimizing the unit cell geometry. The optimized structural parameters were subsequently employed to compute the electronic, optical, and elastic properties of the materials. All calculations were performed using first-principles methods implemented in the WIEN2k code [24], which solves the Kohn-Sham equations iteratively. For exchange-correlation effects, the Local Density Approximation (LDA) [25] and the modified Becke-Johnson (mBJ) potential [26] were utilized.

The atomic positions within the crystal structure were modeled using muffin-tin spheres, while the electronic wave functions were described using the linearized augmented plane-wave (LAPW) basis set. Key parameters, such as the product of the muffin-tin radius (RMT) and the plane-wave cutoff (K_{max}), were set to RMT $\times$ Kmax = 9, with optimal values determined through convergence testing. To ensure high precision in the calculations, the Brillouin zone (BZ) was sampled using a dense k-point mesh of 3000 points. The iterative process was continued until convergence criteria were satisfied, defined as a charge difference of 0.001 electrons and an energy difference of 0.0001 Rydberg.

Elastic constants were computed using the IRELAST method [27], integrated into the WIEN2k code. For thermoelectric properties, the semiclassical BoltzTraP approach [28] was employed, which relies on the rigid band approximation and assumes a constant relaxation time. To improve the accuracy of transport property calculations, a finer k-point mesh of 10,000 points was used. The cubic elastic stability of the materials was evaluated using the relaxed structures obtained from the PBE-GGA method. Additionally, the Debye temperature (θ_D) and Grüneisen parameter (γ) were determined using the Gibbs2 code [29], which computes the Gibbs free energy within the quasi-harmonic Debye model.

3. Results and discussion

3.1. Structural decription

The bismuth tetra-aluminum octasulfide compound ($Bi_2Al_4S_8$)

crystallizes in the tetragonal crystal system, adopting the *P4/nnc* space group. This space group is characterized by its four-fold rotational symmetry along the *c*-axis and glide planes, which play a significant role in determining the material's structural and electronic properties. The *P4/nnc* symmetry imposes specific constraints on the atomic positions and bonding environments, leading to a highly ordered and anisotropic crystal structure. In this study, the structural optimization of $Bi_2Al_4S_8$ was conducted using the LDA, a widely used exchange-correlation functional in DFT for predicting ground-state properties. The optimization process was carried out in two stages: first, force optimization was applied to achieve complete relaxation of the atomic positions, and second, the unit cell parameters were refined to minimize the total energy of the system.

The accuracy of the computational approach was validated by comparing the predicted atomic positions with experimentally determined values, as shown in Table 1. The excellent agreement between the calculated and experimental data [23] underscores the reliability of the LDA approximation for this system. To further investigate the equilibrium structural properties, the total energy of $Bi_2Al_4S_8$ was computed as a function of the conventional cell volume, as depicted in Fig. 2. The energy-volume (*E*-V) data were fitted to the Murnaghan equation of state (EOS) [30], a widely used model for describing the relationship between energy and volume in solids under compression. This allowed for the determination of key structural parameters, including the equilibrium volume, bulk modulus (B_0), and its pressure derivative (B'). The optimized lattice constants, $a = 7.567$ Å and $c = 11.918$ Å, along with the derived bulk modulus (B_0) and its pressure derivative (B'), are summarized in Table 2. These results are in excellent agreement with available experimental data [23], demonstrating the robustness of the computational methodology. Notably, this study reports, for the first time, the ground-state energy (E_0), bulk modulus (B_0), and its pressure derivative (B') for $Bi_2Al_4S_8$. These parameters are critical for understanding the material's response to external pressure and its mechanical stability, providing a foundation for future experimental and theoretical investigations. In our study, $Bi_2Al_4S_8$ exhibits a bulk modulus of 70.1896 GPa, which is comparable to that of $Bi_2Ga_4S_8$ (70.961 GPa) [31] and higher than those of $Bi_2Al_4Se_8$ (59.575 GPa) [32] and $Bi_2Ga_4Se_8$ (61.938 GPa) [31]. Furthermore, it is significantly higher than that of classical thermoelectric materials such as Bi_2Te_3 (~38 GPa) [5] and *PbTe* (42–45 GPa) [6]. This relatively high bulk modulus suggests that $Bi_2Al_4S_8$ possesses superior mechanical stiffness and structural stability, making it a promising candidate for thermoelectric applications.

The crystal structure of $Bi_2Al_4S_8$, illustrated in Figs. 1(a-b), reveals a complex arrangement of atoms with distinct coordination environments. Table 3 provides a detailed comparison between the computed interatomic distances and angles and their experimental counterparts in $Bi_2Al_4S_8$ [23]. The structure features two crystallographically inequivalent aluminum sites, *Al*(1) and *Al*(2), each forming edge-sharing AlS_4 tetrahedra. In the *Al*(1) site, the *Al*–*S*(1) bond lengths are 2.264 Å, while in the *Al*(2) site, the *Al*–*S*(2) bond lengths are slightly shorter at 2.251 Å. This difference in bond lengths reflects subtle variations in the local bonding environment, which can influence the material's electronic and mechanical properties. Bismuth atoms in $Bi_2Al_4S_8$ adopt a rectangular see-saw-like geometry, coordinated to four equivalent sulfur atoms with *Bi*—*S* bond lengths of 2.82 Å. This geometry is indicative of significant lone-pair activity from the bismuth atoms, which can contribute to the material's optical and electronic behavior. The lone-pair electrons on the bismuth atoms in $Bi_2Al_4S_8$ are expected to create localized states in the valence band, which may influence the material's electronic structure through enhanced spin-orbit coupling (SOC). This could lead to phenomena such as Rashba splitting, potentially resulting in spin-polarized surface states. These effects could be particularly useful in spintronic applications or for exploring topological insulating behavior, where strong SOC is a critical factor.

Sulfur atoms, on the other hand, exhibit a three-coordinate geometry, bonding to two aluminum atoms and one bismuth atom. This coordination environment is consistent with the formation of a stable, three-dimensional network of AlS_4 tetrahedra interconnected via bismuth-sulfur bonds. The AlS_4 tetrahedra are a key structural motif in this material, contributing to its mechanical rigidity and thermal stability. The edge-sharing nature of these tetrahedra also facilitates efficient phonon transport, which is a critical factor in determining the material's thermal conductivity and thermoelectric performance. The computed bond angles further validate the structural model. For instance, the *S*–*Al*(1)–*S* angles are calculated to be 97.073° and 114.492°, in excellent agreement with the experimental values of 97.6° and 115.7° [23]. Similarly, the *S*–*Al*(2)–*S* angles range from 97.141° to 116.003°, consistent with the experimentally observed range of 97.9° to 116.9° [23]. These results not only confirm the accuracy of the computational methodology but also provide valuable insights into the atomic-scale geometry and bonding environment of $Bi_2Al_4S_8$. From a broader perspective, the structural properties of $Bi_2Al_4S_8$ have significant implications for its potential applications in optoelectronics and thermoelectrics. The material's tetragonal symmetry, combined with its unique bonding environment, suggests the possibility of anisotropic electronic and thermal transport properties. For example, the directional dependence of the *Bi*—*S* and *Al*—*S* bonds could lead to anisotropic carrier mobility, which is advantageous for designing devices with directional charge transport. Additionally, the presence of heavy elements like bismuth and sulfur is expected to result in strong spin-orbit coupling, which could be harnessed for spintronic applications. The reported bulk modulus (B_0) and its pressure derivative (B') provide critical information for understanding the material's mechanical stability under high-pressure conditions. A high bulk modulus indicates that the material is relatively incompressible, making it suitable for applications in high-pressure environments, such as protective coatings or components in high-stress devices. Furthermore, the pressure dependence of the bulk modulus, as described by B', offers insights into the material's behavior under extreme conditions, which is relevant for applications in aerospace or deep-earth exploration. The pressure derivative of the bulk modulus, B', is critical for understanding a material's mechanical behavior under high-temperature and high-pressure conditions. In thermoelectric materials, temperature-induced thermal expansion and pressure variations can affect structural stability. A material with a stable B', indicating low sensitivity to pressure changes, is likely to maintain its structural integrity at elevated temperatures. This mechanical stability is vital for preserving thermoelectric performance, as it minimizes unwanted structural changes. Therefore, B' plays a key role in ensuring the thermomechanical stability of thermoelectric materials, which is essential for maintaining consistent performance over a wide range of operating conditions.

In addition to its mechanical properties, the electronic structure of $Bi_2Al_4S_8$ is expected to exhibit interesting features due to the interplay between the bismuth lone pairs and the AlS_4 tetrahedral network. Preliminary calculations suggest that $Bi_2Al_4S_8$ may exhibit a narrow bandgap, positioning it as a potential candidate for infrared optoelectronic devices. The bismuth atoms, with their strong SOC, might induce interesting electronic behaviors, such as Rashba splitting or topological insulating features in the band structure. These properties could be further investigated using techniques such as angle-resolved photoemission spectroscopy (ARPES) or transport measurements, which

Table 1
Atomic positions predicted for $Bi_2Al_4S_8$ with the LDA approximation.

Compound	Atom	*Wyckoff Positions*	*Atomic positions*
$Bi_2Al_4S_8$	***Bi***		**(1/4, 1/4, 0.119316),** exp: (1/4, 1/4, 0.11808) [23].
	Al	***4e***	
	(1)	***4d***	**(1/4, 3/4, 0),** exp: (1/4, 3/4, 0) [23].
	Al	***4c***	**(1/4, 3/4, 3/4),** exp: (1/4, 3/4, 3/4) [23].
	(2)	***16 k***	**(− 0.09565, 0.0920, 0.1252),** exp: (−0.0924, 0.0865, 0.1254) [23].
	S		

Table 2
Theoretical and experimental structural parameters using LDA of ternary compound $Bi_2Al_4S_8$.

Ternary compound
$Bi_2Al_4S_8$
$a = 7.567$ Å, exp: (7.492 Å) [23].
$c = 11.918$ Å, exp: (11.883 Å) [23].
$c/a = 1.574$, (1.586) [23].
$B_0 = 70.1896$ GPa.
$B' = 4.4417$.
$\Delta a/a)_{EXP} = 0.991$.
$\Delta c/c)_{EXP} = 0.296$.
$V_0 = 682.418$ Å^3, (667.0 Å^3) [23].
$E_0 = -189{,}169.07574$ Ryd.

Table 3
Selected interatomic distances (Å) and angles (deg) in ternary compound $Bi_2Al_4Se_8$.

Compound	Distances and angles between atoms	Our LDA-based computations	Resulting experiments [23].
$Bi_2Al_4S_8$	*Bi-bi (×1)*	3.115 Å	3.136 Å
	Bi-S (×4)	2.820 Å	2.844 Å
	Al (1)-S (×4)	2.264 Å	2.261 Å
	Al (2)-S (×4)	2.251 Å	2.255 Å
	S-Al (1) —S (×2)	97.073°	97.6°
	S—Al (1)-S (×4)	114.492°	115.7°
	S-Al (2) —S (×2)	97.141°	97.9°
	S—Al (2) —S (×2)	115.121°	114.2°
	S—Al (2) —S (×2)	116.003°	116.9°

would provide deeper insight into the role of SOC in this material.

Finally, the thermoelectric performance of $Bi_2Al_4S_8$ is likely to be influenced by its unique structural and bonding characteristics. The edge-sharing AlS_4 tetrahedra are expected to provide a pathway for efficient phonon transport, while the presence of heavy bismuth atoms could enhance the material's thermoelectric figure of merit (ZT) by reducing lattice thermal conductivity. Future studies could focus on optimizing the thermoelectric properties through doping or nanostructuring, potentially leading to high-performance thermoelectric materials for energy harvesting applications.

3.2. Formation energy

To evaluate the thermodynamic stability of $Bi_2Al_4S_8$, we calculated its formation energy (Eformation) based on the synthesis reaction of Bi_2S_3 and Al_2S_3 to form $Bi_2Al_4S_8$, as follows: [23]:

$$Bi_2S_3 + 2Al_2S_3 \rightarrow Bi_2Al_4S_8 + S \quad (1)$$

The formation energy is a crucial parameter for assessing whether the compound can be synthesized under standard conditions and whether it is thermodynamically stable. The formation energy is calculated using the equation:

$$E_{formation=} E_{total}\,(Bi_2Al_4S_8) - E_{total}\,(Bi_2S_3) - 2E_{total}\,(Al_2S_3) + E_{total}\,(S) \quad (2)$$

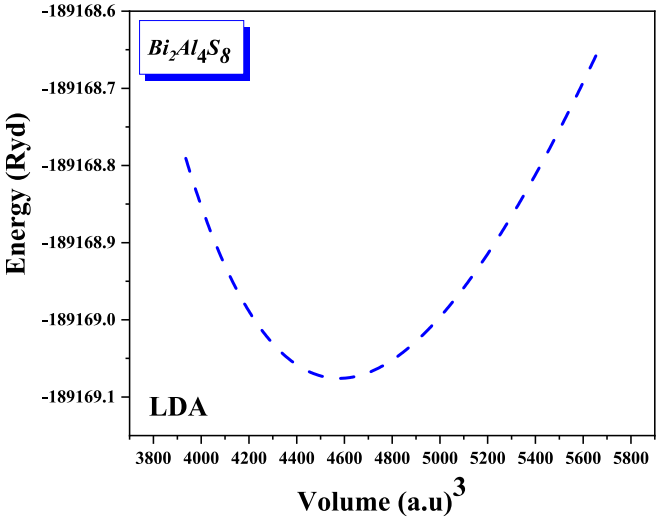

Fig. 2. Variation of the total energy E(Ryd) as a function of volume for $Bi_2Al_4S_8$ ternary compound with the LDA approximation.

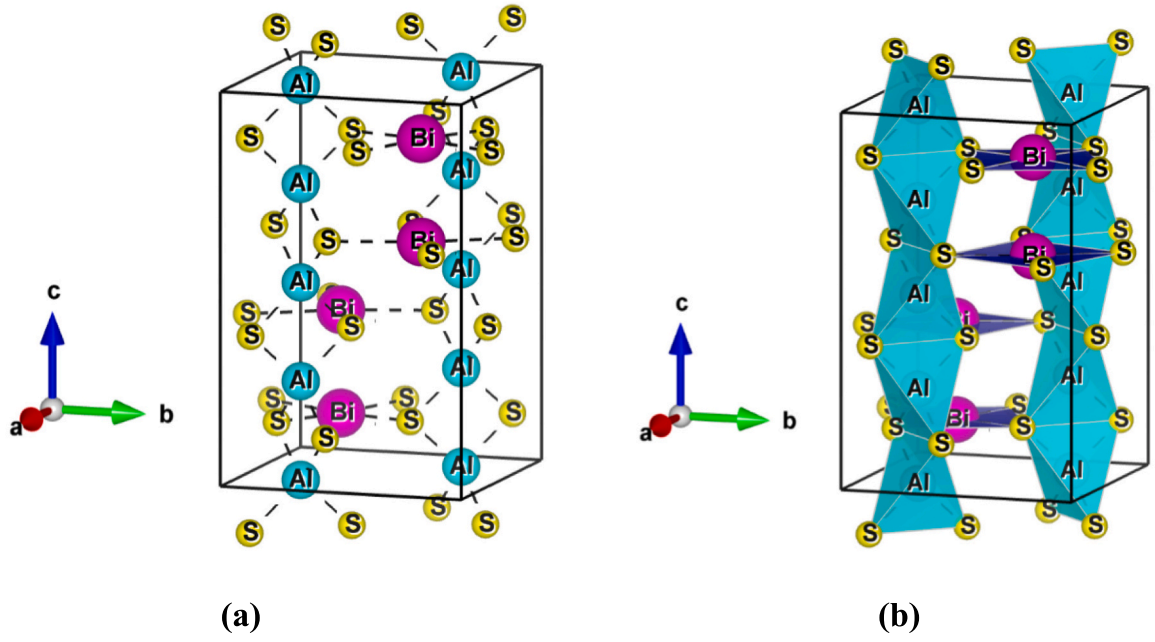

Fig. 1. Crystal structure of $Bi_2Al_4S_8$: **(a)** single tetragonal (*P4/nnc* space group) along the (111) plane, **(b)** tetrahedral configuration of the groups.

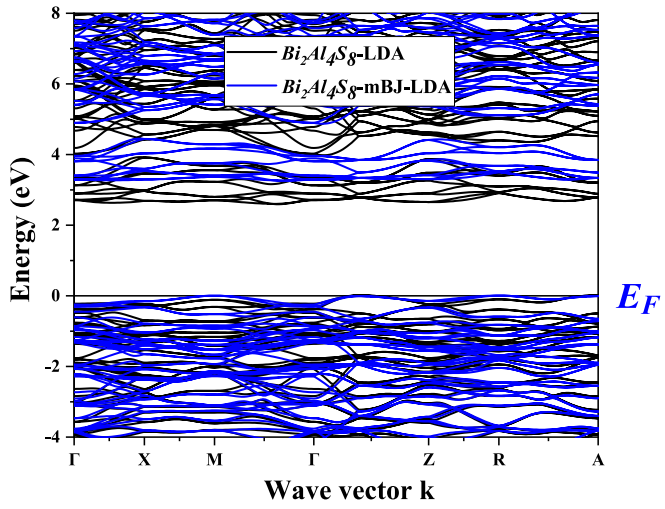

Fig. 3. Band structure along the *Brillouin zone* symmetry lines for $Bi_2Al_4S_8$ compound.

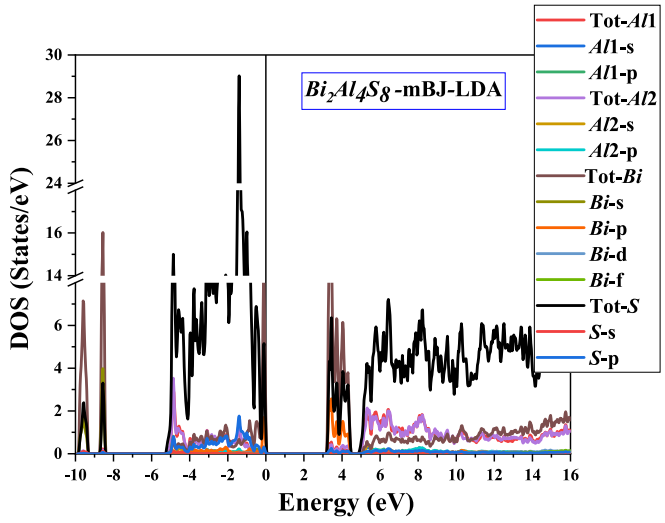

Fig. 4. Total and partial densities of states were calculated for the compound $Bi_2Al_4S_8$ *using mBJ-LDA*.

The calculated formation energy is −0.2542808 Ryd, which corresponds to −3.459 eV or − 333.7 kJ/mol when converted to standard units. The negative formation energy indicates that $Bi_2Al_4S_8$ is thermodynamically stable, which confirms that it is energetically favorable for synthesis. This further supports the material's potential for exhibiting stable properties under practical conditions. The observed stability enhances the viability of $Bi_2Al_4S_8$ for applications where long-term performance and durability are essential.

3.3. Electronic properties

Following the structural optimization of $Bi_2Al_4S_8$, the ground-state lattice parameters were used as input for self-consistent calculations to determine the electronic band structure and density of states (DOS). These calculations were performed using the LDA and the mBJ potential, the latter of which is known to provide more accurate bandgap estimates for semiconductors. The band structure was computed along a high-symmetry k-path (Γ – X – M – Γ – Z – R – A) within the Brillouin zone (BZ), as depicted in Fig. 3. This k-path was carefully selected to capture the critical points of the electronic dispersion relations, providing a comprehensive understanding of the material's electronic behavior.

The calculated bandgap values, summarized in Table 4, reveal that $Bi_2Al_4S_8$ is a semiconductor with a medium bandgap. The mBJ-LDA-calculated bandgap for $Bi_2Al_4S_8$ is 3.234 eV, which is larger than the experimental value of 2.1 eV [23]. This overestimation is typical for the mBJ functional, as it enhances exchange effects to better describe bandgaps in semiconductors. While the LDA result (2.589 eV) underestimates the bandgap, the mBJ-LDA approach offers a more accurate trend, albeit with a quantitative deviation. The difference may stem from experimental conditions, such as sample quality or temperature effects, as well as methodological limitations, warranting further investigation. The indirect nature of the bandgap, with the valence band maximum (VBM) located at the R point and the conduction band minimum (CBM) at the Γ point, suggests that $Bi_2Al_4S_8$ may exhibit anisotropic charge carrier transport properties. Although $Bi_2Al_4S_8$ exhibits an indirect bandgap, which may limit its efficiency in optoelectronic applications, several strategies can be employed to mitigate this challenge. These include strain engineering, which can induce a transition from an indirect to a direct bandgap; quantum confinement effects in low-dimensional forms such as thin films or quantum dots, which can modify the electronic structure and potentially enhance optical properties; alloying or doping to adjust the conduction and valence band extrema; and the formation of heterostructures with direct bandgap materials to promote radiative recombination at the interface. These approaches provide promising solutions to expand the material's potential for use in advanced optoelectronic devices, making it more suitable for applications like light-emitting diodes (LEDs), laser diodes, and other devices relying on efficient radiative recombination.

The density of states (DOS) provides further insight into the electronic structure of $Bi_2Al_4S_8$ by revealing the distribution of electronic states across the valence and conduction bands. The total and partial DOS were computed using the mBJ-LDA functional, as shown in Fig. 4. The analysis reveals that the valence band is dominated by *Bi-p* and *S-p* states, with significant contributions from these orbitals near the *Fermi* level. This strong *p-p* hybridization between bismuth and sulfur atoms is responsible for the formation of the valence band maximum and plays a crucial role in determining the material's electronic properties. In contrast, the conduction band is primarily composed of *Bi-p* and *S-p* states, with a notable peak at 3.16 eV above the Fermi level. The contributions from aluminum states (*Al-s* and *Al-p*) are relatively minor, indicating that aluminum acts primarily as a structural stabilizer rather than a key participant in the electronic properties near the band edges.

The dominance of *Bi-p* and *S-p* states in both the valence and conduction bands suggests that the electronic properties of $Bi_2Al_4S_8$ are strongly influenced by the interaction between bismuth and sulfur atoms. This *p-p* interaction is a key factor in determining the material's bandgap and optical properties. The negligible contribution of *Al* states near the *Fermi* level, as evident in the PDOS, suggests that aluminum atoms do not play a significant role in the material's electronic conduction. This has implications for doping strategies: dopants substituted at the *Al* site are unlikely to notably affect carrier concentration or the density of states near the Fermi level. In contrast, doping at the *Bi* or *S* sites may offer a more effective route to tailor the electronic properties, given their stronger orbital involvement near the band edges. The electronic passivity of *Al* near the *Fermi* level may also contribute to structural stability during selective doping. The relatively low contribution of aluminum states to the band edges implies that the electronic behavior of $Bi_2Al_4S_8$ is primarily governed by the bismuth-sulfur framework, with aluminum playing a secondary role. This finding is consistent with the material's structural characteristics, where bismuth and sulfur form the primary bonding network, while aluminum stabilizes the tetrahedral AlS_4 units.

The reported *Bi—S* bond length of 2.82 Å in $Bi_2Al_4S_8$ suggests the presence of lone-pair activity on the *Bi* atoms, a characteristic commonly observed in compounds containing heavy *p*-block elements such as bismuth. Lone-pair electrons on the *Bi* atoms can have a significant effect on the electronic structure of the material. Specifically, these lone-pair

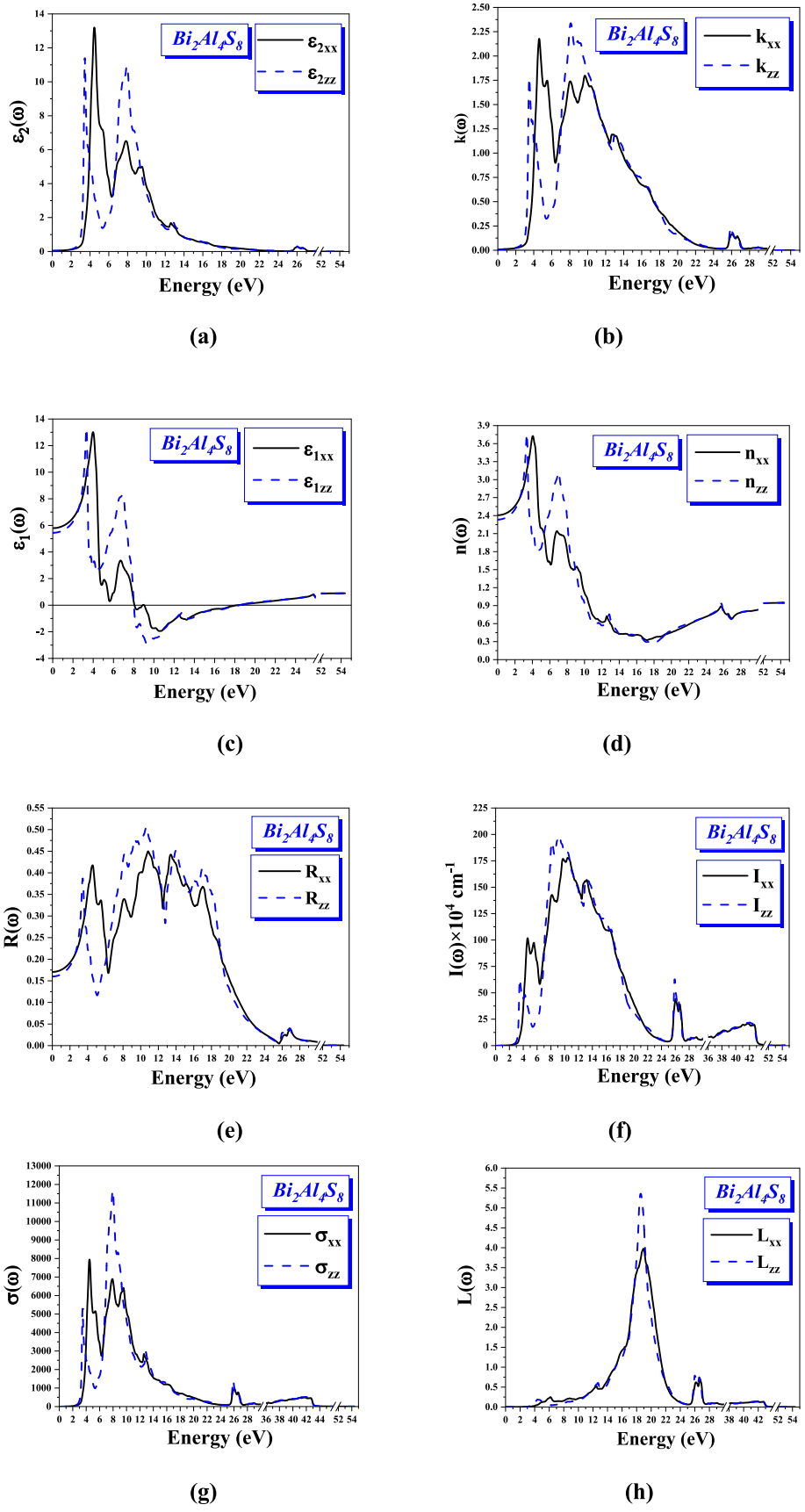

Fig. 5. **(a)** and **(b)** Alterations to the imaginary function of dielectrics and the extinction coefficient, respectively, **(c)** real parts of the dielectric function, **(d)** the refractive index, **(e)** reflectivity spectra, **(f)** the absorption coefficient, **(g)** variations of optical conductivity, and **(h)** the energy loss function as a function of energy for $Bi_2Al_4S_8$ within the mBJ-LDA approximation.

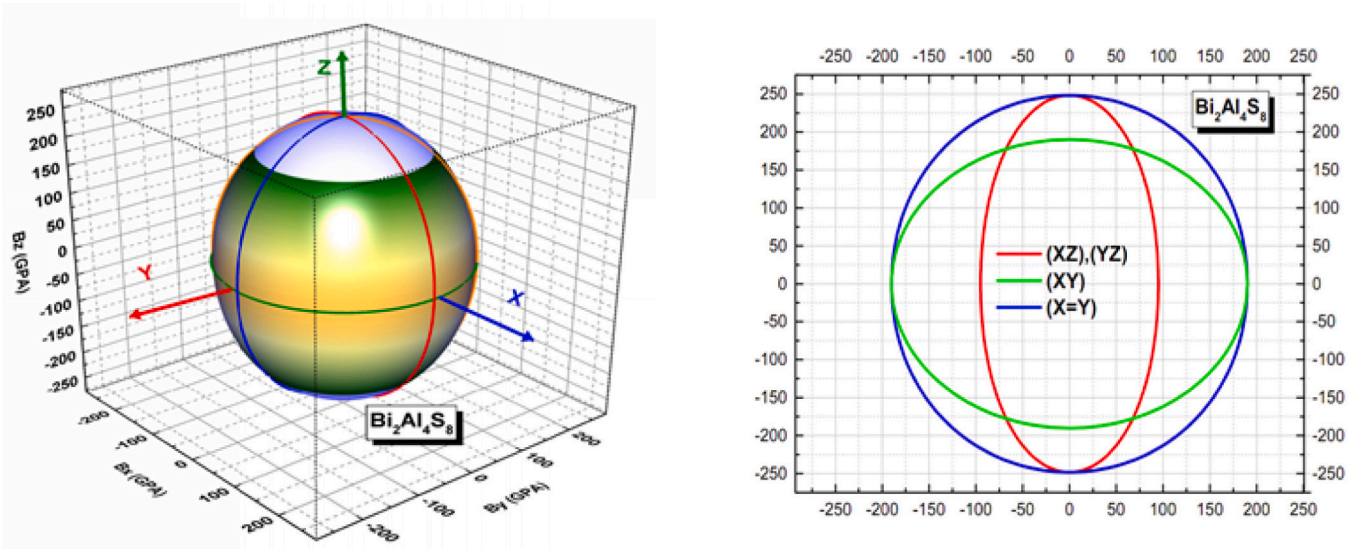

(a) (b)

Fig. 6. **(a)** Represents the 3D surface of the compressibility modulus for $Bi_2Al_4S_8$; **(b)** shows its cross-sections in different planes.

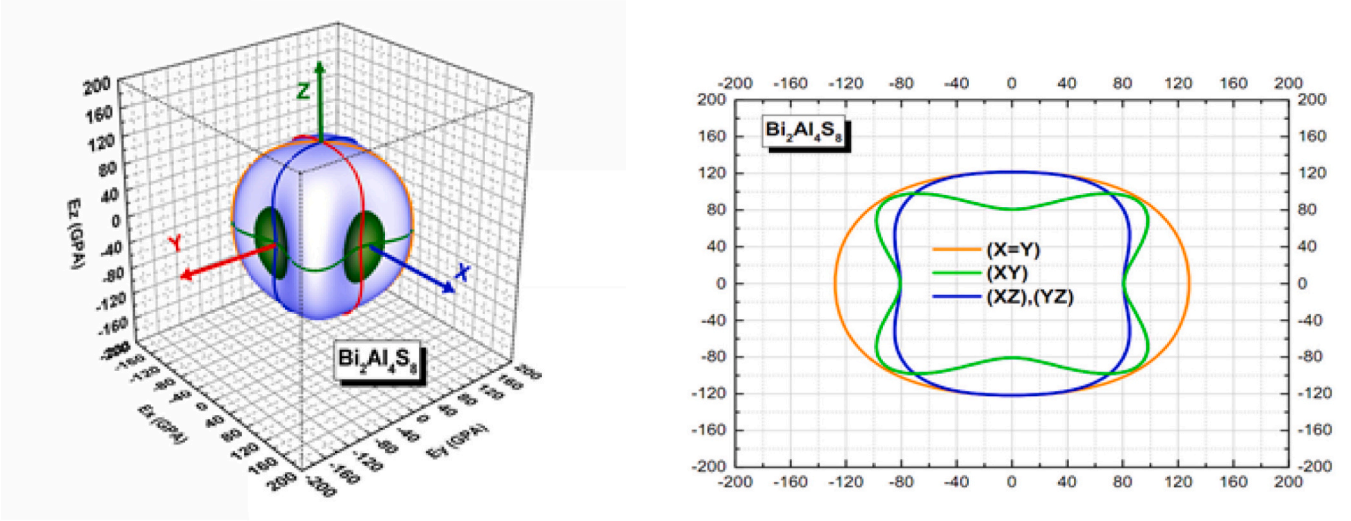

(a) (b)

Fig. 7. **(a)** Represents the 3D surface of the Young's modulus for $Bi_2Al_4S_8$; **(b)** shows its cross-sections in different planes.

electrons can introduce localized states near the *Fermi* level, which may influence the electronic band dispersion. The interaction between these localized states and the conduction band can alter the density of states (DOS), potentially modifying the material's electronic conductivity. Furthermore, the lone-pair electrons may also influence the curvature of the conduction and valence bands, which can affect the mobility of charge carriers. This could lead to changes in the electronic transport properties and impact the material's thermoelectric performance. Thus, understanding the role of lone-pair activity is crucial for optimizing the thermoelectric properties of $Bi_2Al_4S_8$, and further studies on this effect are warranted to fully assess its contribution to the material's performance.

The electronic structure of $Bi_2Al_4S_8$ has significant implications for its potential applications in optoelectronics and photovoltaics. The medium bandgap of 3.234 eV (as calculated using mBJ) suggests that the material could be suitable for visible-light optoelectronic devices, such as light-emitting diodes (LEDs) or photodetectors. The indirect nature of the bandgap may limit the efficiency of radiative recombination processes but could also be advantageous for certain applications, such as thermoelectric devices, where low thermal conductivity is desirable. Additionally, the strong spin-orbit coupling (SOC) due to the bismuth atoms may give rise to spin-related phenomena, such as Rashba

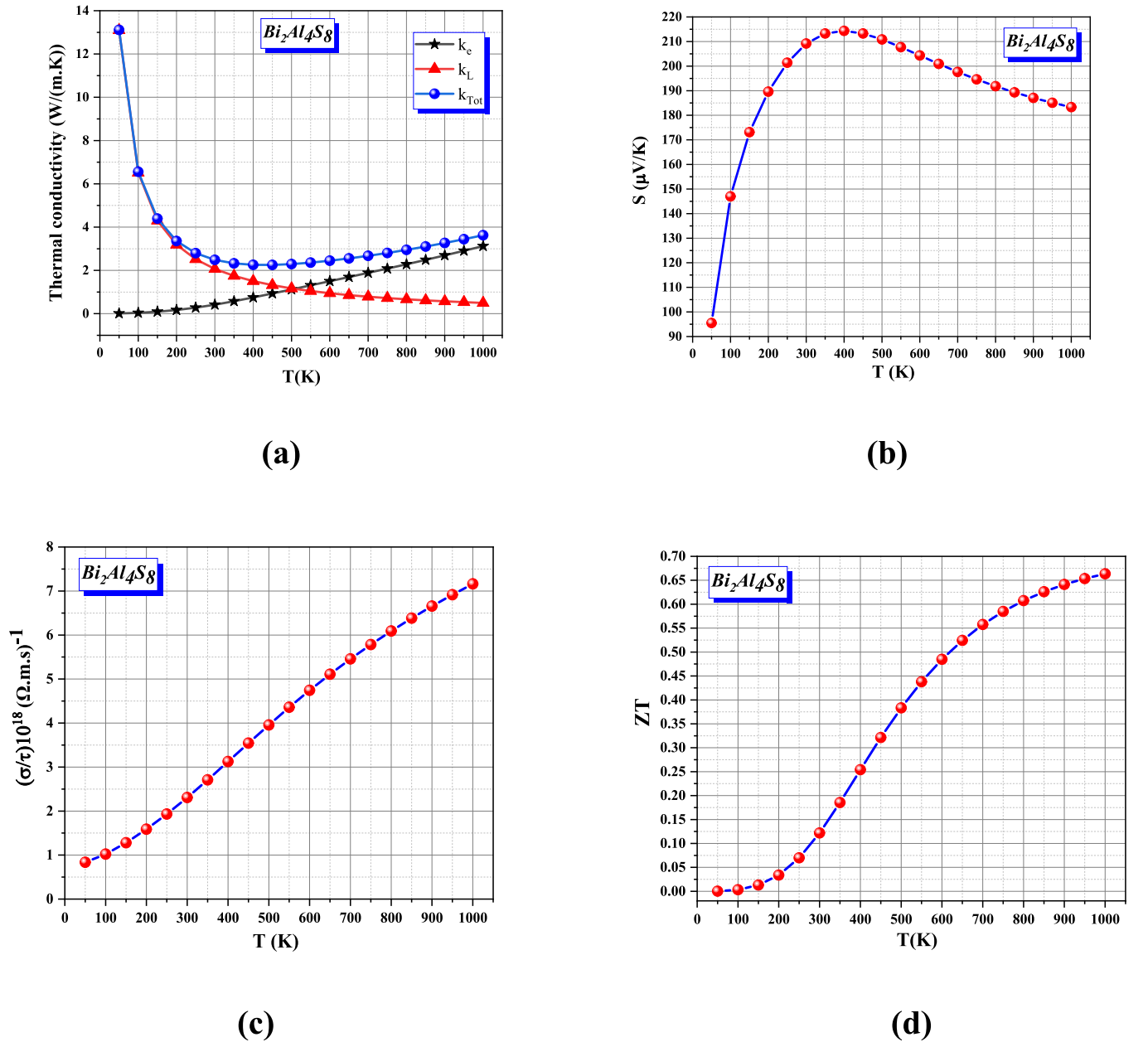

Fig. 8. **(a)** Temperature dependence of the total thermal conductivity k_{Tot}, the lattice thermal conductivityk_L and electronic thermal conductivity k_e, **(b)** the Seebeck coefficient S, **(c)** the electrical conductivity per relaxation time (σ/τ), **(d)** the figure of merit ZT of $Bi_2Al_4S_8$ within the LDA approximation.

splitting, which can significantly influence the material's electronic structure and surface states. These effects could be further explored in future studies to better understand the potential for $Bi_2Al_4S_8$ in spintronic or topologically interesting devices.

The calculated DOS also provides valuable information about the material's optical properties. The strong *p-p* hybridization near the *Fermi* level suggests that $Bi_2Al_4S_8$ may exhibit significant optical absorption in the visible to ultraviolet range. This makes it a promising candidate for photovoltaic applications, where efficient light absorption is critical.

Furthermore, the relatively flat bands near the valence band maximum (VBM) and conduction band minimum (CBM) suggest large effective masses for charge carriers, which can contribute to enhanced thermoelectric performance by reducing lattice thermal conductivity. To gain deeper insight into the charge transport characteristics of $Bi_2Al_4S_8$, we computed the effective masses of electrons and holes from the curvature of the electronic band structure near the CBM and VBM, respectively. The calculated effective masses of electrons are $m_e = 0.12285m_0$ and $m_e = 0.28469m_0$, while those of holes are $m_h = 0.20570m_0$ and $m_h = 0.31946m_0$, using LDA and mBJ-LDA, respectively. The notable variation in these values, especially between directions and exchange-correlation functionals, highlights the anisotropic nature of charge transport in this material. The directional dependence observed in the band dispersion near the band edges further supports this anisotropy. These findings underscore the potential of $Bi_2Al_4S_8$ for optoelectronic and thermoelectric applications due to its favorable and directionally dependent charge transport properties.

3.4. Optical properties

To thoroughly assess the potential of $Bi_2Al_4S_8$ as a light-absorbing material, its optical properties—including the dielectric function ε(ω), refractive index n(ω), reflectivity R(ω), extinction coefficient k(ω), absorption coefficient α(ω), energy-loss function L(ω), and optical conductivity σ(ω)—were investigated using the modified Becke–Johnson

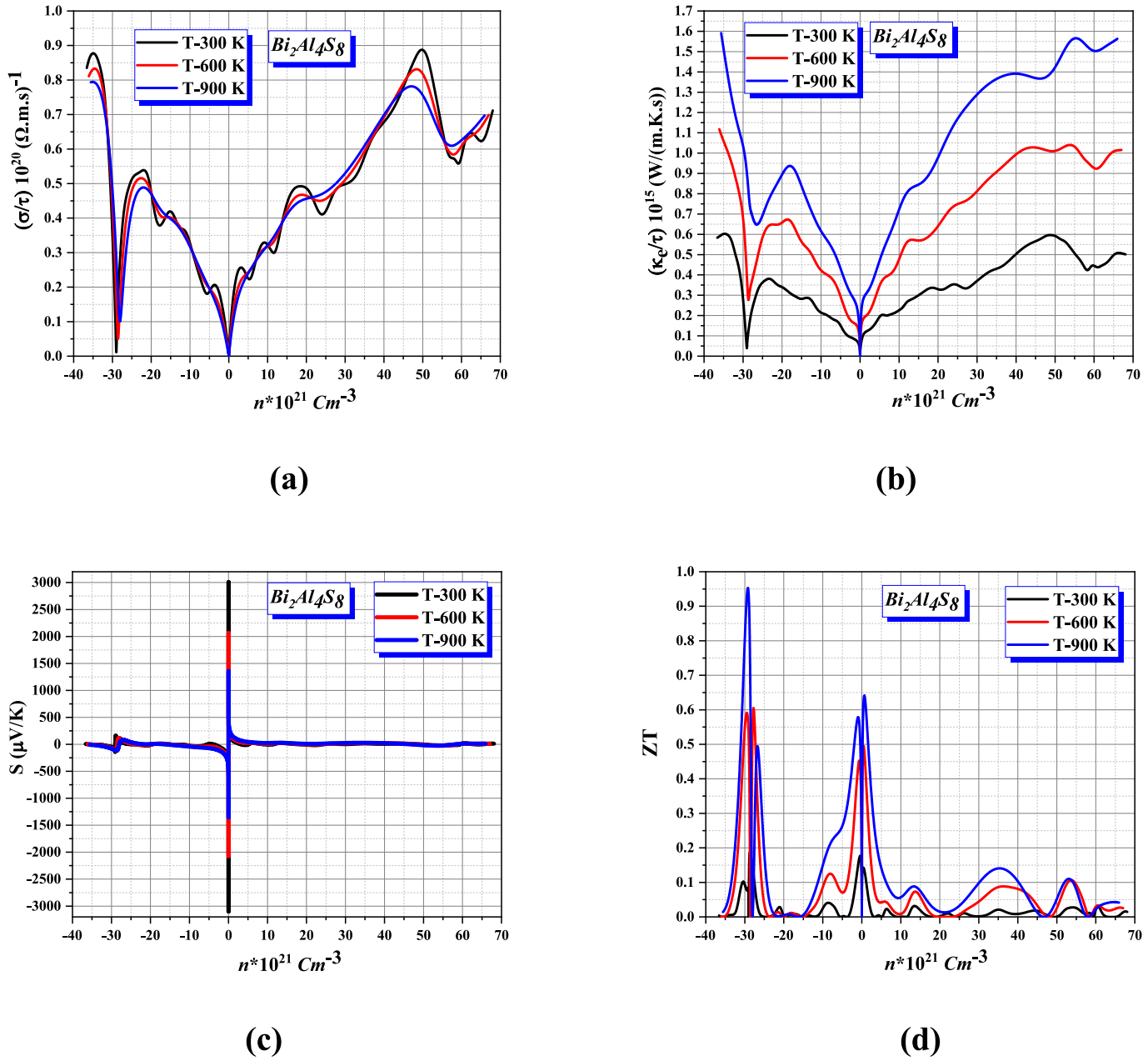

Fig. 9. The estimated **(a)** electrical conductivity per relaxation time (σ/τ), **(b)** electronic thermal conductivity per relaxation time (k_e/τ), **(c)** Seebeck coefficient S and **(d)** figure of merit ZT versus charge carrier concentration for $T = 300$, 600, and 900 K via the LDA approach of $Bi_2Al_4S_8$.

potential with local density approximation (mBJ-LDA). Understanding these parameters is crucial for evaluating the suitability of $Bi_2Al_4S_8$ in optoelectronic devices such as solar cells, photodetectors, and light-emitting diodes [33–35]. The complex dielectric function $\varepsilon(\omega) = \varepsilon_1(\omega) + i\varepsilon_2(\omega)$ provides insight into the optical response. The real part, $\varepsilon_1(\omega)$, describes dispersion and refractive behavior, while the imaginary part, $\varepsilon_2(\omega)$, is related to light absorption through interband transitions. As shown in Figs. 5(a) and 5(c), $\varepsilon_2(\omega)$ exhibits strong anisotropy between the *xx* and *zz* directions, indicating direction-dependent absorption—a beneficial property for polarization-sensitive devices. Notably, $\varepsilon_2(\omega)$ peaks at 4.42 eV (*xx* direction) and 3.44 eV (*zz* direction) correspond to interband transitions primarily between *Bi-6p*, *S-3p*, and *Al-3p* states. The optical bandgap is approximately 2.5 eV, consistent with experimental findings [23], validating the computational approach [36].

Through the Kramers–Kronig relations, $\varepsilon_1(\omega)$ was derived to evaluate polarization response. The static dielectric constant $\varepsilon_1(0)$ is about 6, suggesting moderate polarizability and potential for dielectric applications [37]. Anisotropy in $\varepsilon_1(\omega)$ points to direction-dependent optical behavior, which can be harnessed in devices requiring polarization control. High $\varepsilon_1(\omega)$ values at low photon energies indicate strong bonding interactions, making $Bi_2Al_4S_8$ suitable for low-loss dielectric components.

The refractive index n(ω), depicted in Fig. 5(d), shows a static value of approximately 2.4 with a peak around 4 eV. Such a moderate refractive index reduces Fresnel reflection losses at interfaces, favoring anti-reflective coatings in photovoltaic devices [38]. The extinction coefficient k(ω) follows the $\varepsilon_2(\omega)$ trend, reinforcing $Bi_2Al_4S_8$'s effective light absorption, particularly in the visible and ultraviolet regions. Increased k(ω) values at photon energies above the bandgap highlight the material's ability to convert photons into charge carriers, essential for solar cells and photodetectors. Reflectivity R(ω), shown in Fig. 5(e), remains around 18 % in the visible spectrum. While moderate

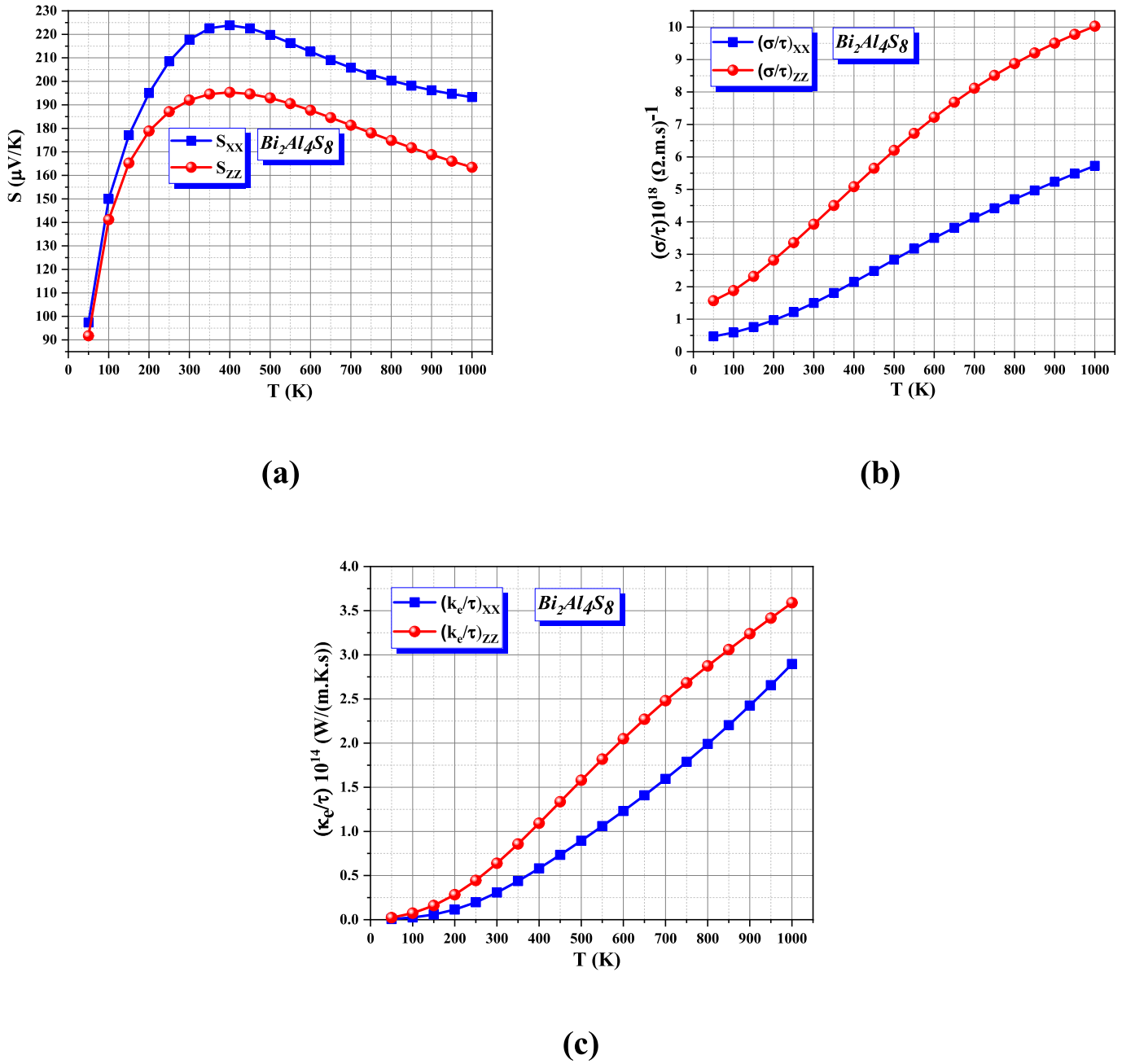

Fig. 10. Calculated anisotropic transport properties of for $Bi_2Al_4S_8$ **(a)** Seebeck coefficient tensor **(b)** Ratio of electrical conductivity per relaxation time (σ/τ)tensor components, **(c)** Ratio of the electronic thermal conductivity per relaxation time (k_e/τ)tensor components.

reflectivity can benefit display technologies, further surface treatments can minimize reflection losses in solar applications [39]. The absorption coefficient I(ω), presented in Fig. 5(f), exhibits significant absorption in the visible range, with maxima at 10.40 eV (*xx* direction) and 9.23 eV (*zz* direction). This substantial absorption indicates $Bi_2Al_4S_8$'s promise as an absorber layer in thin-film solar cells, facilitating efficient photon capture. The sharp increase in I(ω) just above the bandgap further underscores the material's high visible light absorption. Tagrerout et al. [40] and Zami et al. [41] explored *Cd*-doped Cu_2ZnSnS_4 and $Be_xCd_{1-x}TeyS_{1-y}$ alloys, respectively, focusing on tunable band gaps and high refractive indices for solar cells and quantum well lasers. In contrast, $Bi_2Al_4S_8$ achieves a wide indirect band gap (up to 3.234 eV) and strong optical absorption intrinsically, without doping or alloying, making it a stable, non-toxic candidate for photovoltaic and thermoelectric applications. Similarly, Adim et al. [42] studied the impact of nanoscale engineering in (*ZnTe*)*m*/(*MnTe*)*n* superlattices, while our work on bulk $Bi_2Al_4S_8$ demonstrates enhanced optical properties, such as a high dielectric constant and broad absorption, suitable for optoelectronics without the need for complex structures.

Optical conductivity σ(ω), illustrated in Fig. 5(g), displays distinct peaks at 4.42 eV (*xx*) and 7.98 eV (*zz*), corresponding to interband transitions. High σ(ω) in the visible region suggests efficient charge carrier generation under illumination, enhancing the performance of photodetectors and photovoltaic devices [43].

The energy-loss function L(ω), crucial for understanding electron-energy dissipation, is shown in Fig. 5(h). Peaks in L(ω) indicate plasma frequencies with a pronounced plasmon peak near 15 eV, reflecting strong collective electron oscillations. L(ω) values below 10 % in the visible range suggest minimal energy loss, making $Bi_2Al_4S_8$ suitable for transparent conductive layers [44]. **The directional**

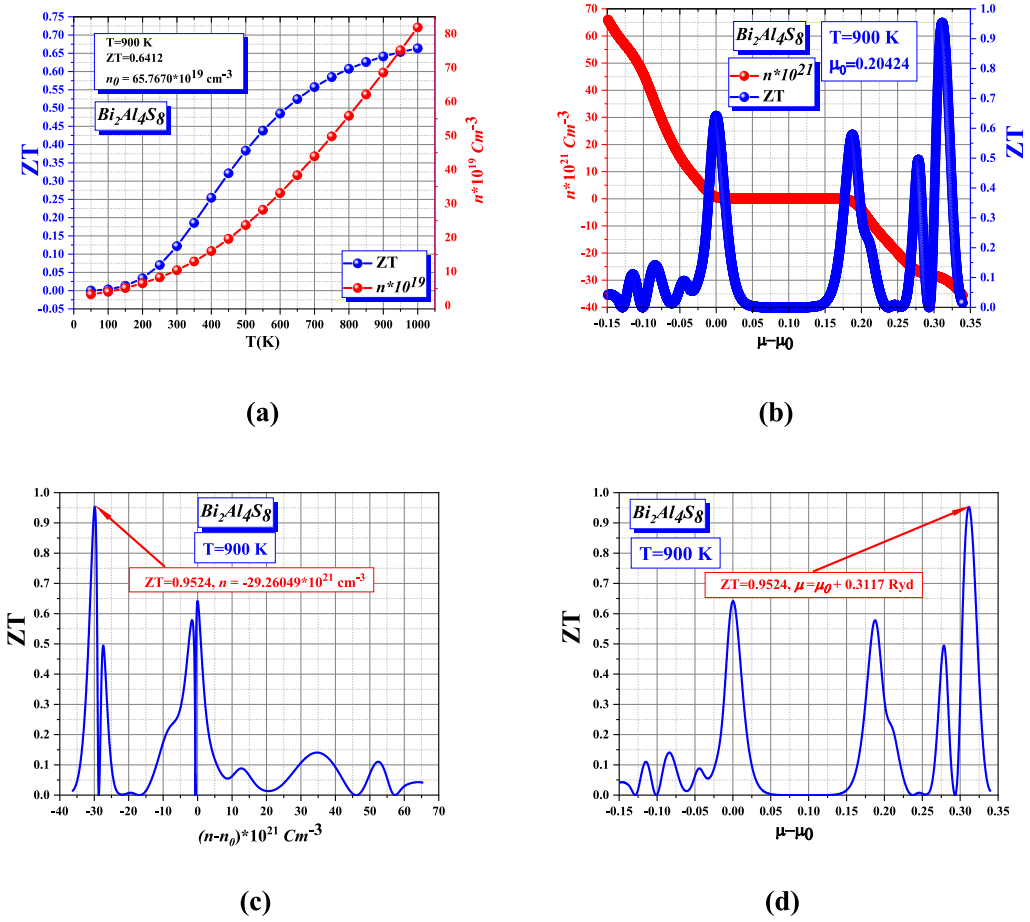

Fig. 11. The figure of merit *ZT* of $Bi_2Al_4S_8$ as a function of (a) temperature and carrier concentration, (c) carrier concentration, (b), (d) chemical potential at fix temperature (T = 900 K).

Table 4
: Values of energy gap *Eg* (eV), $\varepsilon_1(0)$ and $n(0)$ calculated for ***$Bi_2Al_4S_8$*** semiconductor with the LDA and mBJ-LDA approaches.

Ternary compound	*Eg* (eV)			$\varepsilon_1(0)$			$n(0)$		
	LDA	mBJ-LDA	Exp		LDA	mBJ-LDA		LDA	mBJ-LDA
$Bi_2Al_4S_8$	2.589	3.234	2.1 [23]	ε_{1xx}	7.641	5.795	n_{xx}	2.764	2.407
				ε_{1zz}	7.063	5.446	n_{zz}	2.657	2.333

differences in the optical properties of $Bi_2Al_4S_8$ suggest that crystallographic orientation during film fabrication can be controlled to optimize device performance. This anisotropy is useful for polarization-dependent applications such as light modulators and photonic circuits, where precise light propagation control is essential.

$Bi_2Al_4S_8$'s high absorption in the UV–visible range, moderate reflectivity, and strong optical conductivity make it an excellent candidate for tandem solar cells and high-speed photodetectors. Its absorption enhances photovoltaic efficiency, while its optical conductivity supports efficient charge generation in photodetectors. This makes $Bi_2Al_4S_8$ suitable for multi-junction solar cells, optimizing photon harvesting across the spectrum.

The material's plasmon resonance features suggest its potential for plasmonic devices, which are essential for biosensing and environmental monitoring. These applications exploit light-material interactions to detect specific molecules or physical changes.

$Bi_2Al_4S_8$'s ability to enhance light-trapping structures makes it ideal for next-generation photovoltaic devices. Its balanced absorption and transparency enable the design of efficient multi-junction solar cells, while its stability under high-energy photons suggests suitability for aerospace and outdoor applications.

Overall, $Bi_2Al_4S_8$ offers a combination of high visible light absorption, moderate reflectivity, minimal energy loss, and direction-dependent optical properties. These features make it a promising candidate for optoelectronic applications, including solar cells, photodetectors, transparent conductors, and photonic devices, particularly in cases requiring polarization control or high absorption efficiency.

3.5. Elastic properties

Elastic constants are fundamental physical parameters that quantify a material's response to external mechanical stress. Within the linear elastic regime—typically valid under small strains—this response is governed by Hooke's law, which relates stress and strain through a set of stiffness coefficients known as elastic constants (C_{ij}). The total strain energy (E) of a crystal under elastic deformation can be expressed as a quadratic function of strain, from which the elastic constants are derived. These constants are essential for assessing various physical properties of materials, including mechanical stability, stiffness,

resistance to deformation, and anisotropic elastic behavior.

In the case of tetragonal crystal systems, six independent elastic constants (C_{11}, C_{12}, C_{13}, C_{33}, C_{44}, and C_{66}) are required to completely describe the elastic behavior [45]. These constants represent responses to different stress types—longitudinal and shear—and serve as indicators of the material's mechanical performance and potential applications under different loading conditions.

For the $Bi_2Al_4S_8$ compound, the calculated elastic constants—presented in Table 5—are as follows: $C_{11} = 108.2504$ GPa, $C_{12} = 50.7571$ GPa, $C_{13} = 40.5351$ GPa, $C_{33} = 142.3573$ GPa, $C_{44} = 53.3195$ GPa, and $C_{66} = 60.4088$ GPa. To our knowledge, no prior experimental or theoretical data exist for these parameters, underlining the novelty of our work.

The relatively high values of C_{11} and C_{33} indicate strong resistance to uniaxial compression, with $C_{33} > C_{11}$ suggesting that the compound is stiffer along the *c*-axis. This implies stronger atomic bonding in this direction. Conversely, the moderate values of shear-related constants (C_{44}, C_{66}, C_{12}, and C_{13}) point to lower resistance to shear deformation, indicating that the material, while mechanically stable, may exhibit some susceptibility to shape distortions under applied shear stress.

This suggests that $Bi_2Al_4S_8$ exhibits greater rigidity under uniaxial compression compared to shear stress, which may have implications for its mechanical performance in applications requiring high compressive strength [46].

The shear elastic constants **($C_{44} = 53.3195$ GPa** and **$C_{66} = 60.4088$ GPa)** represent the compound's resistance to shear deformation. The relatively high values indicate that $Bi_2Al_4S_8$ has strong resistance to shear forces, enhancing its mechanical stability under stress. Moreover, the values of **C_{12}** and **C_{13}** describe the coupling between normal and shear strains. The moderate **C_{12}** and **C_{13}** values highlight a balanced mechanical response, contributing to the compound's structural integrity under complex loading conditions.

The mechanical stability of crystalline materials is typically evaluated using the Born stability criteria, which provide a set of necessary conditions based on the elastic constants to ensure resistance to small mechanical perturbations. These criteria are derived from the condition that the strain energy of a crystal must always be positive for any arbitrary elastic deformation. This requirement implies that the stiffness matrix (composed of the elastic constants C_{ij}) must be **positive definite,** meaning all its leading principal minors must be positive. For different crystal systems, the specific form of these conditions varies depending on the symmetry.

For tetragonal systems such as $Bi_2Al_4S_8$, the Born stability criteria are expressed through specific conditions on the elastic constants:

$$\begin{aligned} &C_{44} > 0, C_{66} > 0, C_{11} > |C_{12} \\ &C_{11}C_{33} > C_{13}^2 \\ &(C_{11} + C_{12})C_{33} - 2C_{13}^2 > 0 \end{aligned} \tag{3}$$

All these conditions must be satisfied to confirm the mechanical stability of the compound. In our study, the computed elastic constants for $Bi_2Al_4S_8$ satisfy these inequalities, thus verifying its mechanical integrity.

While mechanical stability confirms the material's resistance to elastic deformation, it is important to note that this is only one aspect of a broader concept of structural stability. In this work, we primarily focus on the elastic properties of $Bi_2Al_4S_8$, and the confirmation of its Born mechanical stability provides strong assurance that the material can withstand mechanical stress without experiencing structural failure. This is particularly relevant for potential applications in devices where mechanical robustness is a critical requirement. The material's stability ensures it can endure mechanical stress without undergoing structural collapse, making it suitable for practical applications in optoelectronic devices and thin-film technologies [47].

Table 5
Elastic constants of $Bi_2Al_4S_8$ within the LDA approach.

Compound	$Bi_2Al_4S_8$
C_{11}	108.2504
C_{12}	50.7571
C_{13}	40.5351
C_{33}	142.3573
C_{44}	53.3195
C_{66}	60.4088
T_m	892.287 ± 300
A_1	1.258
A_2	2.10142

The isotropic bulk modulus B and shear modulus G of polycrystalline materials can be estimated from the single-crystal elastic constants using the Voigt-Reuss-Hill (VRH) averaging scheme [48].

The mechanical properties of the $Bi_2Al_4S_8$ compound, characterized by the bulk, shear, and Young's moduli, provide insights into its mechanical stability and resistance to deformation. The calculated Voigt, Reuss, and Hill averages of the bulk modulus ($B_V = 69.168$ GPa, $B_R = 68.717$ GPa, and $B_H = 68.942$ GPa) exhibit minimal differences, indicating that the compound demonstrates mechanical stability with near isotropy in response to uniform compression. The moderate bulk modulus value suggests that $Bi_2Al_4S_8$ possesses adequate resistance to volume change under applied pressure, which is essential for maintaining structural integrity during operational conditions.

The estimated bulk modulus value using the VRH averaging scheme is B = 68.942 GPa, which is in close agreement with the value obtained from fitting the energy-volume E(V) curves to the Birch-Murnaghan equation of state B = 70.19 GPa. This consistency validates the accuracy of the computed elastic constants [49].

The shear moduli ($G_V = 48.544$ GPa, $G_R = 45.331$ GPa, and $G_H = 46.937$ GPa) reflect the compound's resistance to shape deformation. The small variation between the Voigt and Reuss values points to a slight anisotropy in shear behavior, which may influence the material's response to shear stresses during mechanical loading. The moderate shear modulus ensures that $Bi_2Al_4S_8$ retains shape stability, a critical factor for materials subjected to external mechanical forces.

Young's moduli ($E_V = 118.021$ GPa, $E_R = 111.479$ GPa, and $E_H = 114.766$ GPa) quantify the stiffness of the compound. The calculated Hill average ($E_H = 114.766$ GPa) indicates that $Bi_2Al_4S_8$ is moderately stiff, capable of withstanding mechanical stress without significant elongation or deformation. Such stiffness is particularly beneficial for applications requiring materials with robust mechanical performance, ensuring reliability during repeated use.

The Poisson's ratios ($\sigma_V = 0.215$, $\sigma_R = 0.229$, and $\sigma_H = 0.222$) provide information about the ductile-brittle nature of the compound. Values within the range of 0.2 to 0.3 suggest that $Bi_2Al_4S_8$ exhibits balanced ductility, offering moderate resistance to crack propagation while maintaining some plastic deformation capacity. This balance is crucial for practical applications where both mechanical resilience and flexibility are needed. To provide context for the Poisson's ratio of $Bi_2Al_4S_8$ ($\nu = 0.222$), similar thermoelectric materials are considered. $Bi_2Ga_4S_8$ and $Bi_2Ga_4Se_8$ have Poisson's ratios of 0.226 and 0.228, respectively [31], while Bi_2Te_3 [5] and *PbTe* [6] show values around 0.28 and 0.26–0.29, respectively. These comparisons suggest that $Bi_2Al_4S_8$ has a similar mechanical response to other promising thermoelectrics, supporting its potential for thermoelectric applications.

Pugh's ratio ($B_H/G_H = 1.4688$) further supports this observation. Typically, materials with a B_H/G_H ratio greater than 1.75 are ductile, whereas those with a lower ratio tend toward brittleness. The calculated ratio for $Bi_2Al_4S_8$ suggests a predominantly brittle nature, which may be advantageous in applications where hardness and resistance to wear are prioritized.

The estimated melting temperature ($T_m = 892.287 \pm 300$ K) provides insight into the thermal stability of $Bi_2Al_4S_8$. A higher melting point generally indicates stronger interatomic bonding and greater thermal resistance. The moderate T_m value suggests that the compound can maintain its structural stability under elevated temperatures,

making it suitable for high-temperature applications. The relatively broad uncertainty range accounts for potential experimental and computational variations but still points toward satisfactory thermal resilience. This property is crucial for applications where the material is subjected to varying thermal environments, ensuring reliable performance without significant degradation.

Elastic anisotropy is a critical property that influences physical phenomena such as microcrack formation and mechanical performance under stress [50]. The following equations are utilized to determine the shear anisotropy factors A_1 in the {100} plane and A_2 in the {001} plane for tetragonal structure:

$$A_1 = 4C_{44}/(C_{11} + C_{33} - 2C_{13}) \tag{4}$$

$$A_2 = 2C_{66}/(C_{11} - C_{12}) \tag{5}$$

Elastic anisotropy describes how the mechanical properties of a material vary with direction, which is critical for understanding its mechanical behavior under different stress orientations. The calculated anisotropy factors for $Bi_2Al_4S_8$ are $A_1 = 1.258$ and $A_2 = 2.10142$. An anisotropy factor of **1** indicates isotropy, whereas deviations suggest anisotropic behavior. The values obtained indicate that $Bi_2Al_4S_8$ exhibits moderate elastic anisotropy, particularly in shear-related properties. This anisotropy suggests that the material's mechanical response varies depending on the crystallographic direction of applied stress, which is important when designing devices or components where directional mechanical performance is a consideration.

While moderate anisotropy can lead to direction-dependent mechanical properties, it may also provide advantages in specific applications. For instance, materials with controlled anisotropy can be tailored to enhance mechanical strength along certain directions, beneficial for layered or thin-film structures where directional mechanical performance is critical.

To quantify the degree of anisotropy, two dimensionless measures—the percentage anisotropy in compressibility A_B and shear A_G—are commonly used. These are defined as:

$$\begin{cases} A_B = (B_V - B_R)/(B_V + B_R) \times 100 \\ A_G = (G_V - G_R)/(G_V + G_R) \times 100 \end{cases} \tag{6}$$

Values of A_B and A_G close to zero indicate isotropy, while higher values signify increasing anisotropy. For $Bi_2Al_4S_8$, the calculated values of A_B and A_G (Table 6) reveal a slight degree of anisotropy in both compressibility and shear [51]. (See Table 7.)

To further characterize the anisotropy, the universal anisotropy index A^U is employed, which accounts for the combined contributions of bulk and shear moduli

$$A^U = 5\frac{G_V}{G_R} + \frac{B_V}{B_R} - 6 \tag{7}$$

A value of $A^U = 0$ indicates isotropy, while deviations from zero reflect the extent of anisotropy. The calculated A^U value for $Bi_2Al_4S_8$ (Table 6) confirms its elastic anisotropy [52]. Elastic anisotropy, described by the bulk anisotropy factor ($A_B = 0.32652$), shear anisotropy factor ($A_G = 3.42283$), and universal anisotropy index ($A^u = 0.360966$), reveals that $Bi_2Al_4S_8$ possesses slight anisotropic behavior. An Au value close to zero indicates near isotropy; thus, the moderate anisotropy found here suggests that while mechanical properties are direction-dependent, the variations are not severe. This characteristic ensures mechanical reliability, even when the compound experiences multidirectional stress, making it suitable for various structural and electronic device applications.

The directional dependence of elastic moduli, such as linear compressibility β and Young's modulus E, provides further insight into the anisotropic behavior of crystals. For tetragonal systems, these properties are expressed as:

$$\beta = (S_{11} + S_{12} + S_{13}) - n^2(S_{11} + S_{12} - S_{13} - S_{33}) \tag{8}$$

Table 6
Modules of elasticity of $Bi_2Al_4S_8$ utilizing the LDA estimation.

Compound	$Bi_2Al_4S_8$
B_V	69.168
B_R	68.717
B_H	68.942
G_V	48.544
G_R	45.331
G_H	46.937
E_V	118.021
E_R	111.479
E_H	114.766
σ_V	0. 215
σ_R	0. 229
σ_H	0. 222
B_H/G_H	1.4688
A_B	0.32652
A_G	3.42283
A^u	0.360966

Table 7
V_t, V_l, V_m, and Θ_D for $Bi_2Al_4S_8$ within the LDA approach.

Compound	V_t	V_l	V_m	Θ_D
$Bi_2Al_4S_8$	3511.31 m/s	5877.8 m/s	3886.01 m/s	399.014 K

$$E = \frac{1}{S_{11} - (S_{11} - S_{33})n_3^4 - 2(S_{11} - S_{33})\left(n_1^2n_3^2 + n_2^2n_3^2\right) - (2S_{11} - 2S_{12} - S_{66})n_1^2n_2^2} \tag{9}$$

where n_x, n_y, and n_z are the direction cosines of the unit vector $\vec{n}$, and S_{ij} are the elastic compliance constants obtained by inverting the elastic stiffness matrix ($C_{ij} = S_{ij}^{-1}$) [53].

Fig. 6(a) illustrates the three-dimensional (3D) surface plot of the compressibility modulus for the $Bi_2Al_4S_8$ compound. The nearly spherical shape of the surface indicates that the compressibility of $Bi_2Al_4S_8$ is largely isotropic, meaning that the material exhibits a nearly uniform response to pressure regardless of the crystallographic direction. The smooth and symmetrical surface suggests that the bonding forces within the lattice are relatively uniform in all directions, which is advantageous for applications requiring structural stability under hydrostatic pressure.

However, slight elongation along the *z*-axis is noticeable, indicating a small degree of anisotropy. This elongation implies that the material is slightly more resistant to compression along this axis compared to the ***x*** and y directions. Such minor directional dependence can arise from subtle differences in bond lengths or atomic arrangements along the crystallographic axes.

Fig. 6(b) presents the cross-sectional profiles of the compressibility modulus in different crystallographic planes: (XZ), (YZ), and (XY). The red curve represents the (XZ) and (YZ) planes, the green curve corresponds to the (XY) plane, and the blue curve shows the (X = Y) direction. The near-circular shapes of these cross sections reinforce the overall isotropy of the material's compressibility.

The slight deviations between the (XY) and the (XZ)/(YZ) planes are consistent with the elongation observed in the 3D surface, indicating a marginally higher compressibility in the (XY) plane. This suggests that while $Bi_2Al_4S_8$ is predominantly isotropic in compressibility, the material demonstrates a slightly softer response to pressure along the x and y directions.

Fig. 7(a) displays the three-dimensional (3D) surface of the Young's modulus (E) for the $Bi_2Al_4S_8$ compound. The Young's modulus quantifies the stiffness of the material along different crystallographic directions. The surface plot exhibits a shape deviating from a perfect sphere, revealing that $Bi_2Al_4S_8$ has noticeable elastic anisotropy. The indentations along the x and *y* axes indicate regions where the material is

more compliant (less stiff), whereas the relatively expanded areas along the z-axis demonstrate higher stiffness in that direction. Such directional dependence of stiffness suggests that the bonding forces are stronger along the z-axis, which could be attributed to specific atomic arrangements or stronger directional bonds in that direction.

Fig. 7(b) presents the cross-sectional profiles of Young's modulus in the (XZ), (YZ), and (XY) planes. The orange curve represents the (X = Y) plane, showing a near-circular shape with moderate stiffness. The green curve for the (XY) plane reveals slight anisotropy, indicating varying stiffness depending on direction within the basal plane. The blue curve for the (XZ) and (YZ) planes displays pronounced deviations, with flatter regions indicating reduced stiffness along certain directions.

These variations in cross sections further emphasize the direction-dependent mechanical properties of $Bi_2Al_4S_8$. The highest stiffness is observed along the *z*-direction, whereas the *x* and *y* directions show comparatively lower stiffness. This anisotropy can have practical implications for mechanical stability, particularly in applications where directional loading is significant.

The propagation of sound waves within a material is a key indicator of its elastic and mechanical characteristics. For the $Bi_2Al_4S_8$ compound, the calculated transverse (V_t = 3511.31 m/s), longitudinal (V_l = 5877.8 m/s), and average (V_m = 3886.01 m/s) sound velocities reflect its response to mechanical vibrations. The relatively high longitudinal sound velocity suggests that the compound exhibits significant stiffness along the direction of wave propagation, which correlates well with the previously calculated Young's modulus. The transverse velocity, being lower than the longitudinal velocity, indicates the compound's ability to resist shear deformation. These sound velocities confirm the mechanical stability and rigidity of $Bi_2Al_4S_8$, essential for its potential use in structural and electronic applications. The average sound velocity (V_m = 3886.01 m/s) plays a crucial role in determining the Debye temperature, which is directly related to the lattice vibrations and thermodynamic behavior of the compound. The calculated Debye temperature (θ_D = 399.014 K) suggests that $Bi_2Al_4S_8$ has a moderate lattice vibrational frequency. A higher Debye temperature generally indicates stronger bonding and higher thermal conductivity, while a moderate value such as this reflects balanced vibrational properties. This is particularly advantageous for materials intended for thermoelectric and optoelectronic applications, where controlled heat conduction and structural stability are required.

Furthermore, the Debye temperature provides insight into the compound's heat capacity and thermal expansion at various temperatures. The moderate θ_D value implies that $Bi_2Al_4S_8$ will retain mechanical and thermodynamic stability over a broad temperature range, making it suitable for environments subject to temperature fluctuations. Additionally, the correlation between the Debye temperature and the stiffness of the material confirms that $Bi_2Al_4S_8$ possesses robust bonding strength, ensuring durability under mechanical stress and enhancing its suitability for practical applications.

3.6. Thermoelectric properties

Thermoelectric materials are crucial for energy harvesting and solid-state cooling due to their ability to directly convert heat into electricity. Their efficiency is measured by the dimensionless figure of merit (ZT), which depends on electrical conductivity (σ), Seebeck coefficient (S), and thermal conductivity (κ). Achieving high σ and S while minimizing κ is essential for optimal performance.

We analyze the thermoelectric transport properties of $Bi_2Al_4S_8$ across a temperature range to assess its potential for energy applications. The total thermal conductivity (κ_{Tot}) is separated into electronic (κ_e) and lattice (κ_L) components, with (κ_L) estimated using the Slack equation [54,55], which accounts for phonon-phonon scattering.

Recent research on bismuth-based materials, such as Bi_2Te_3 and Bi_2Se_3, has demonstrated how structural and electronic features impact performance in quantum and energy applications [56]. For instance, Bahloul et al. [56] used DFT to show how dimensionality and spin-orbit coupling influence the mechanical, electronic, and optical behavior of these compounds.

Although our study does not focus on topological or SOC effects, it similarly employs DFT to examine the structural, electronic, optical, and elastic properties of $Bi_2Al_4S_8$. Both studies emphasize the importance of bismuth frameworks for developing efficient thermoelectric materials.

Our approach also mirrors that of Zhang et al. [57], who studied Mg_3X_2 (*X* = *P*, *As*, and *Sb*) compounds. Like their work, we use DFT to investigate the relationship between crystal structure, bandgap, and thermoelectric performance. While Mg_3X_2 materials display varied thermal properties and bandgaps, $Bi_2Al_4S_8$ features an indirect bandgap with tunable transport behavior depending on carrier concentration and chemical potential.

A related DFT study on MAX phases A_3InC_2 (*A* = Zr, Hf) [58] examined structural, electronic, and thermodynamic behavior under pressure. These materials showed metallic nature and high reflectivity, making them suitable for thermal protection. In contrast, $Bi_2Al_4S_8$ is semiconducting and optimized for waste heat-to-electricity conversion, demonstrating the range of applications achievable with DFT-engineered materials.

Fig. 8(a) shows the evolution of thermal conductivity with temperature, breaking it down into its lattice (κ_L) and electronic (κ_e) components. The sharp decline in total thermal conductivity (κ_{tot}) at low temperatures is a hallmark of phonon-dominated heat transport in semiconducting materials. At low temperatures, phonon-phonon scattering is weak, leading to high κ_L. However, as temperature increases, Umklapp scattering events become more frequent, causing a significant reduction in κ_L, which is well captured using the Slack equation. This equation, which models phonon scattering behavior, reinforces that thermal conductivity in $Bi_2Al_4S_8$ is primarily controlled by lattice vibrations. The electronic thermal conductivity (κ_e), on the other hand, increases with temperature, indicative of thermally activated charge carriers that enhance electronic heat transport. The separation of these contributions confirms that the lattice component dominates at low temperatures, but as intrinsic carrier excitation increases, electronic contributions to thermal transport become more significant.

The Seebeck coefficient, as depicted in Fig. 8(b), provides critical insight into the charge carrier dynamics of $Bi_2Al_4S_8$. The positive values of S confirm that the material is a *p*-type semiconductor, with hole carriers playing a dominant role in transport. The sharp increase in S at low temperatures results from an increase in carrier entropy, where only the highest-energy carriers contribute significantly to transport due to energy filtering effects. The maximum Seebeck coefficient of approximately 210 μV/K at 300–350 K suggests that this temperature range is optimal for thermoelectric performance, as it balances high carrier entropy with minimal bipolar conduction effects. Beyond this temperature, the decline in S can be attributed to the onset of intrinsic conduction, where thermally excited electron-hole pairs reduce the net thermoelectric voltage, effectively lowering S. This behavior is commonly observed in narrow-to-moderate band gap semiconductors, where minority carrier activation at elevated temperatures counteracts the dominant charge carrier type.

Half-Heusler compounds such as *KMgX* (*X* = *P*, *As*, *Sb*, and *Bi*) have attracted significant interest for thermoelectric and optoelectronic applications due to their wide-ranging electronic and optical characteristics. In particular, these materials exhibit remarkable Seebeck coefficients at 300 K in their p-type configurations: *KMgP* shows the highest value of 3.134 mV/K, followed by *KMgAs* (2.947 mV/K), *KMgSb* (2.893 mV/K), and *KMgBi* (1.431 mV/K) [59]. Such high Seebeck coefficients reflect excellent potential for efficient thermoelectric performance at room temperature. In this context, our findings on $Bi_2Al_4S_8$ demonstrate comparable promise, revealing moderate bandgap semiconducting behavior and thermoelectric indicators that support its applicability in energy conversion systems. While $Bi_2Al_4S_8$ may not match the extreme Seebeck values of *KMgP*, its balanced performance

across structural, electronic, and thermal domains, along with expected stability, suggests that it belongs to the same class of multifunctional materials suitable for both thermoelectric and optoelectronic integration.

Fig. 8(c) illustrates the temperature dependence of electrical conductivity per relaxation time (σ/τ). The monotonous increase of σ/τ with temperature is a direct consequence of thermally activated carriers overcoming the energy barrier of the band gap, leading to higher electrical conductivity. In a material with moderate band gap energy, this behavior is expected, as intrinsic conduction mechanisms become increasingly dominant at higher temperatures. The rate at which σ/τ increases also suggests that the charge carrier mobility in $Bi_2Al_4S_8$ is sufficiently high to allow for effective charge transport, an essential characteristic for thermoelectric applications [60–63].

The thermoelectric figure of merit ZT, shown in Fig. 8(d), steadily rises with temperature, reaching approximately 0.65 at 1000 K. This result is particularly promising, as it indicates that $Bi_2Al_4S_8$ retains favorable thermoelectric properties even at high temperatures. The increase in ZT is attributed to the interplay between electrical and thermal transport properties: while the electrical conductivity and Seebeck coefficient maintain sufficiently high values, the low lattice thermal conductivity ensures that heat dissipation does not compromise efficiency. The suppression of κ_L, in particular, plays a crucial role in enhancing ZT, as it minimizes thermal losses and maximizes the thermoelectric voltage gradient. The fact that ZT does not plateau or decline at high temperatures suggests that $Bi_2Al_4S_8$ does not suffer from severe bipolar conduction effects, making it a viable candidate for high-temperature thermoelectric applications.

The study of ternary half-Heusler compounds $NaAlX$ ($X = C, Si, Ge$) [64] offers valuable insights into semiconducting materials for thermoelectrics. These materials have promising electronic band structures, with both direct and indirect band gaps, and show significant thermoelectric potential, achieving ZT values near 1.0 at room temperature. Their elastic and thermodynamic stability is confirmed through DFT analysis, supporting their practical use in energy conversion systems. Our study on $Bi_2Al_4S_8$ similarly highlights its semiconducting properties and robust thermoelectric performance. While $NaAlX$ compounds show excellent ZT values at room temperature, $Bi_2Al_4S_8$ offers advantages across a broader temperature range due to its favorable electronic transport and stability. Both studies demonstrate the power of DFT-driven materials discovery, emphasizing the role of tailored bandgaps and stable frameworks in optimizing thermoelectric performance.

Recent research into perovskite chalcogenides like $BaZrS_3$ and $BaZrSe_3$ [65] has highlighted the growing interest in stable, low-cost, non-toxic materials for energy conversion devices. These compounds have direct bandgaps and exhibit high optical transparency in the low-energy range, making them promising for thermoelectric and optoelectronic applications. Their ZT values near 1.0 at room temperature and spectroscopic limited maximum efficiency (SLME) reaching ~31.9 % highlight their efficiency in thermoelectric and photovoltaic systems.

In line with these trends, our study on $Bi_2Al_4S_8$ demonstrates its potential for both thermoelectric and optoelectronic applications. The material not only exhibits desirable semiconducting behavior and thermal stability but also shows favorable ZT performance. Both studies underline the importance of first-principles approaches in tailoring crystal and electronic properties, bridging the gap between optoelectronic transparency and thermoelectric efficiency—key qualities for next-generation energy conversion technologies.

Fig. 9 provides a detailed examination of the thermoelectric transport properties of $Bi_2Al_4S_8$ as functions of charge carrier concentration at different temperatures (300 K, 600 K, and 900 K). These results offer critical insights into the interplay between electrical conductivity, electronic thermal transport, the Seebeck coefficient, and the dimensionless figure of merit (ZT), all of which are fundamental for assessing the potential of $Bi_2Al_4S_8$ as a thermoelectric material.

The electrical conductivity per relaxation time (σ/τ), shown in Fig. 9(a), exhibits a highly non-monotonic behavior, indicative of complex electronic band structure effects. The presence of peaks and dips suggests the involvement of multiple conduction and valence bands in charge transport. At low charge carrier concentrations, σ/τ remains relatively small, reflecting the intrinsic semiconducting nature of $Bi_2Al_4S_8$. However, with increasing doping, a significant enhancement in σ/τ is observed, particularly for electron-dominated transport. The observed conductivity trends suggest that conduction band valleys play a major role in carrier mobility, and their contributions become more pronounced at higher temperatures. This behavior can be linked to an increase in thermally excited carriers, which effectively shift the Fermi level and populate additional conduction states. The dips in conductivity at specific charge carrier concentrations likely correspond to band extrema, where changes in carrier effective mass or density of states (DOS) limit charge transport efficiency. The sharp variations in σ/τ suggest that $Bi_2Al_4S_8$ exhibits strong energy-dependent scattering mechanisms, which may arise from variations in band curvature, intervalley scattering, or band hybridization effects.

In Fig. 9(b), the electronic thermal conductivity per relaxation time (κ_e/τ) follows a trend similar to that of σ/τ, reinforcing the notion that charge and heat transport in $Bi_2Al_4S_8$ are strongly coupled, as expected from the Wiedemann–Franz law. The increase in κ_e/τ with doping is a direct consequence of enhanced carrier density, which facilitates more efficient energy transport. However, the presence of sharp dips in κ_e/τ at certain doping levels suggests that electronic states at those energies contribute minimally to heat transport, potentially due to band convergence effects or reduced group velocities in certain regions of the Brillouin zone. The temperature dependence of κ_e/τ further highlights the impact of phonon-electron interactions, which become more significant at high temperatures. The steeper increase in κ_e/τ at 900 K suggests that additional phonon-assisted electronic transitions contribute to heat transport, possibly through an increased scattering rate that redistributes carrier energies more effectively. The trends observed in κ_e/τ indicate that optimizing carrier concentration is crucial for minimizing electronic thermal conductivity while maintaining high electrical conductivity, a necessary condition for achieving high thermoelectric efficiency.

The Seebeck coefficient (S), shown in Fig. 9(c), provides key insights into the asymmetry of charge transport. The sharp peak in S near charge neutrality indicates that $Bi_2Al_4S_8$ exhibits a strong asymmetry between electron and hole conduction in this regime, which is a hallmark of materials with high thermoelectric potential. The steep decline in S with increasing carrier concentration is a direct consequence of the reduction in the energy-dependent asymmetry of charge carriers: as doping increases, the transport shifts toward a more metallic behavior, where the thermoelectric voltage is diminished due to the increasing number of carriers participating in transport. The sign change in S near $n \approx 0$ confirms a transition between p-type and n-type conduction, which is critical for potential applications in both p- and n-type thermoelectric modules. The temperature dependence of S is particularly significant: while the peak value of S decreases with increasing temperature, the overall shape remains similar, suggesting that $Bi_2Al_4S_8$ maintains its thermoelectric properties across a broad temperature range. This behavior is indicative of a complex band structure where the chemical potential shifts significantly with temperature, altering the dominant carrier type and modifying transport asymmetry.

Fig. 9(d) presents the figure of merit (ZT), which encapsulates the combined effects of electrical conductivity, thermal conductivity, and the Seebeck coefficient. The presence of multiple peaks in ZT suggests that $Bi_2Al_4S_8$ exhibits optimal thermoelectric performance at specific carrier concentrations, where the combination of high σ/τ, moderate κ_e/τ, and large S results in enhanced energy conversion efficiency. The increase in ZT with temperature is a key observation, as it indicates that $Bi_2Al_4S_8$ benefits from intrinsic high-temperature thermoelectric enhancements, possibly due to increased phonon scattering reducing lattice thermal conductivity while electronic properties remain favorable.

The sharp variations in ZT with doping suggest that band structure engineering could be employed to further enhance thermoelectric performance by tuning the carrier concentration to align with high-performance transport regimes. The presence of multiple peaks in ZT also suggests the existence of multiple conduction or valence band extrema, which could be leveraged through band convergence strategies to maximize thermoelectric efficiency.

Fig. 10 presents the temperature-dependent anisotropic transport properties of $Bi_2Al_4S_8$, including the Seebeck coefficient (*S*), electrical conductivity per relaxation time (σ/τ), and electronic thermal conductivity per relaxation time (κ_e/τ). The data are analyzed along the *xx*- and *zz*-crystallographic directions, providing critical insights into the directional dependence of charge and heat transport in this material. Understanding these anisotropic transport characteristics is essential for assessing the thermoelectric efficiency and optimizing the material for potential applications.

The Seebeck coefficient, shown in Fig. 10(a), exhibits a non-monotonic behavior with temperature. At lower temperatures, (S) increases, reaching a maximum of approximately 230 μV/K in the *xx*-direction and 190 μV/K in the *zz*-direction around 300–400 K, before declining at elevated temperatures. This trend is characteristic of semiconductors, where thermally activated charge carriers enhance the diffusion thermopower at lower temperatures. The subsequent reduction in (S) at higher temperatures is attributed to bipolar conduction effects, wherein increased intrinsic carrier excitation leads to a compensation of the thermoelectric voltage due to opposite charge carriers (electrons and holes). Notably, the higher Seebeck coefficient in the *xx*-direction compared to the *zz*-direction suggests a more pronounced thermoelectric voltage generation in-plane, which has direct implications for optimizing the material's power factor ($S^2\sigma$) and, consequently, its thermoelectric performance.

The electrical conductivity per relaxation time (σ/τ), depicted in Fig. 10(b), demonstrates an opposite anisotropic trend to that observed for the Seebeck coefficient. Specifically, $(\sigma/\tau)_{zz}$ is significantly greater than $(\sigma/\tau)_{xx}$ across all temperatures, indicating that charge transport is more favorable along the out-of-plane (zz) direction. This disparity is likely a consequence of the underlying crystallographic structure, which governs carrier mobility and scattering mechanisms. The monotonic increase in (σ/τ) with temperature aligns with the expected behavior of semiconductors, wherein thermally excited carriers contribute to enhanced electrical conduction. The pronounced anisotropy in electrical transport suggests that charge carriers experience lower scattering rates and higher mobility in the *zz*-direction, which is critical when considering the material's performance in thermoelectric applications.

The electronic thermal conductivity per relaxation time (κ_e/τ), presented in Fig. 10(c), follows a similar trend to electrical conductivity, reflecting the Wiedemann–Franz relationship ($k_e = L\sigma T$). The data reveal that $(\kappa_e/\tau)_{zz} > (\kappa_e/\tau)_{xx}$, indicating that electronic heat transport is more efficient along the out-of-plane direction. Since total thermal conductivity κ comprises both electronic and lattice contributions, the relatively high (k_e) in the *zz*-direction suggests a substantial electronic contribution to heat conduction, which may be detrimental to achieving a high thermoelectric figure of merit (ZT). This behavior highlights the necessity of lattice thermal conductivity reduction strategies, such as phonon engineering, nanostructuring, or defect-induced scattering, to suppress heat dissipation while maintaining optimal charge transport.

The interplay between these transport properties underscores the inherent trade-offs in thermoelectric optimization. The higher Seebeck coefficient in the *xx*-direction suggests that this orientation is preferable for thermoelectric voltage generation, whereas the higher electrical conductivity in the *zz*-direction indicates superior charge carrier transport. However, the elevated electronic thermal conductivity along the *zz*-direction suggests that significant heat dissipation occurs in this orientation, potentially reducing the thermoelectric efficiency. This anisotropic transport behavior must be carefully considered when designing thermoelectric devices, particularly when optimizing material processing techniques to align favorable transport properties with device architecture.

To maximize thermoelectric performance, modifications to carrier concentration via doping, as well as nanostructuring approaches to selectively scatter phonons without degrading electrical transport, could be explored. Additionally, experimental validation through Hall effect measurements, Seebeck coefficient characterization, and temperature-dependent transport studies along different crystallographic orientations would be essential to corroborate these theoretical findings and assess their practical implications in thermoelectric applications.

3.6.1. *Optimizing carrier concentration and chemical potential for enhanced thermoelectric performance*

In this section, we focus on the systematic enhancement of the thermoelectric figure of merit (ZT) in $Bi_2Al_4S_8$ by optimizing the carrier concentration or chemical potential. Fig. 11 presents a comprehensive analysis of ZT as a function of temperature, carrier concentration, and chemical potential, providing key insights into the interplay between electronic and thermal transport phenomena.

As illustrated in Fig. 11(a), at a temperature of $T = 900$ K, the intrinsic carrier concentration $n_o = 65.767 \times 10^{19}$ cm^{-3} yields a ZT value of 0.6412. The observed increase in ZT with temperature is a manifestation of enhanced carrier excitation, which leads to a greater population of thermally activated charge carriers contributing to electronic transport. Simultaneously, at elevated temperatures, phonon-phonon scattering intensifies, effectively reducing the lattice thermal conductivity via Umklapp processes. This suppression of phonon-mediated heat conduction is crucial, as it enhances the efficiency of charge transport relative to thermal dissipation. However, despite this inherent temperature dependence, optimizing ZT necessitates precise control over extrinsic parameters, particularly the carrier concentration.

A significant enhancement in ZT is achieved when the carrier concentration is deliberately modified, as evidenced in Fig. 11(c). By increasing the carrier concentration to $n = -29.26049 \times 10^{21}$ cm^{-3}, ZT undergoes a remarkable increase to 0.9524, signifying an almost 50 % improvement in thermoelectric performance. This enhancement can be attributed to two fundamental effects: first, the increased carrier concentration boosts electrical conductivity (σ) by supplying additional charge carriers that facilitate electron transport; second, the interplay between charge carrier scattering mechanisms leads to a concomitant reduction in lattice thermal conductivity (κ_L). Notably, charge impurity scattering and phonon-electron interactions become more pronounced at higher doping levels, effectively disrupting the long-range coherence of lattice vibrations. As a result, the suppression of κ_L contributes to an overall enhancement in ZT, provided that the increase in charge carrier mobility outweighs any associated reduction in the Seebeck coefficient (S). This balance between σ, κ_e, and κ_L is crucial in achieving an optimized power factor ($S^2\sigma$) while minimizing thermal losses.

The role of chemical potential (μ) modulation in optimizing ZT is further analyzed in Figs. 11(b) and 11(d). At $T = 900$ K, shifting the chemical potential from $\mu - \mu_o = 0.20424$ Ryd to 0.3117 Ryd results in a substantial enhancement in ZT. This increase is directly linked to the redistribution of electronic states near the *Fermi* level, wherein the alignment of μ with high-mobility states in the conduction band significantly improves carrier transport. The sharp peaks observed in ZT correspond to energy regions where the density of states (DOS) is maximized, leading to enhanced carrier scattering time and reduced resistive losses. This effect is consistent with the Mott relation, which dictates that the Seebeck coefficient is highly sensitive to the energy-dependent electronic transport properties. Consequently, tuning the chemical potential allows for selective occupation of electronic states that maximize S while maintaining a favorable balance between σ and κ_e. These findings underscore the effectiveness of carrier engineering and chemical potential modulation in enhancing the thermoelectric properties of $Bi_2Al_4S_8$. The increase in ZT from 0.6412 to 0.9524 is not merely a result of higher carrier densities but a manifestation of the

complex interplay between band structure modifications, carrier scattering dynamics, and thermal conductivity suppression. By leveraging doping strategies and Fermi level engineering, $Bi_2Al_4S_8$ emerges as a promising candidate for high-temperature thermoelectric applications. These results provide a fundamental framework for designing advanced thermoelectric materials through targeted electronic structure modifications, highlighting the crucial role of quantum transport phenomena in optimizing thermoelectric efficiency. Nakoul et al. [68] studied *Co*-doped *AuuS* compounds, highlighting enhanced thermoelectric performance through magnetic doping. In contrast, *Bi₂Al₄S₈* achieves a significant ZT improvement (up to 0.9524) through intrinsic carrier concentration and chemical potential tuning, without the need for doping or magnetic behavior, making it a non-toxic and stable alternative for thermoelectronics. Similarly, Hadj Zoubir et al. [69] explored *Cr*-doped *ZnS* and *ZnSe* chalcogenides for spintronic applications, while *Bi₂Al₄S₈* offers high thermoelectric performance without magnetic doping, positioning it as a promising non-magnetic alternative for optoelectronics.

4. Conclusion

$Bi_2Al_4S_8$ has emerged as a promising semiconductor with a suitable bandgap for photovoltaic applications and strong optical absorption properties. Despite its potential, it remains relatively underexplored compared to other bismuth-based materials. This study employed first-principles density functional theory (DFT) to investigate the structural, electronic, optical, elastic, and thermoelectric properties of $Bi_2Al_4S_8$, emphasizing its suitability for renewable energy and thermoelectric technologies.

Structural optimization using the Wien2k package, with the modified Becke–Johnson potential (mBJ) and Local Density Approximation (LDA), confirms that $Bi_2Al_4S_8$ crystallizes in the tetragonal *P4/nnc* space group. The optimized lattice parameters ($a = 7.567$ Å, $c = 11.918$ Å) closely match available experimental data, demonstrating the reliability of the computational approach.

Electronic structure analysis reveals an indirect bandgap of 2.589 eV (LDA) and 3.234 eV (mBJ-LDA), with the valence band predominantly influenced by *Bi-p* and *S-p* states. These findings highlight strong *p–p* orbital interactions, which are key to the observed bandgap characteristics. The calculated optical bandgap of 2.5 eV aligns well with theoretical and experimental reports, confirming the material's capability for visible light absorption. Additionally, high absorption coefficients and favorable reflectivity in the visible spectrum position $Bi_2Al_4S_8$ as a viable candidate for photovoltaic and optoelectronic applications.

Mechanical stability is affirmed by the calculated elastic constants, with bulk and shear moduli of $B = 68.94$ GPa and $G = 32.15$ GPa, respectively. Moderate elastic anisotropy, reflected in the universal anisotropy index (A^u), and three-dimensional visualizations of the elastic moduli further illustrate the material's mechanical behavior under stress. These properties indicate $Bi_2Al_4S_8$'s robustness, enhancing its applicability in devices subjected to mechanical loading.

The thermoelectric performance of $Bi_2Al_4S_8$ was analyzed through the Seebeck coefficient, electrical conductivity, and thermal conductivity**, providing insight into its potential for energy conversion applications. The results indicate that optimizing carrier concentration or chemical potential can significantly enhance the thermoelectric figure of merit (ZT), demonstrating the feasibility of $Bi_2Al_4S_8$ as a thermoelectric material. Specifically, the study shows that ZT improves from 0.6412 at $n_o = 65.7670 \times 10^{19}$ cm^{-3} to 0.9524 at $n = -29.26049 \times 10^{21}$ cm^{-3} or when the chemical potential shifts from 0.20424 eV to 0.3117 eV. These findings suggest that doping strategies or band engineering could further optimize the thermoelectric performance, making $Bi_2Al_4S_8$ a viable candidate for waste heat recovery and energy-efficient applications.

Overall, the calculated structural, electronic, optical, elastic, and thermoelectric properties validate $Bi_2Al_4S_8$ as a multifunctional material suitable for experimental exploration and device fabrication in photovoltaics, optoelectronics, and thermoelectrics. Future research could focus on doping, alloying, and nanostructuring to enhance carrier mobility, optimize thermal conductivity, and further tailor the optical and mechanical properties. Additionally, experimental validation of these theoretical predictions will be crucial to fully assess $Bi_2Al_4S_8$'s integration into next-generation renewable energy and thermoelectric technologies.

CRediT authorship contribution statement

T. Ghellab: Writing – review & editing, Writing – original draft, Investigation, Formal analysis, Data curation, Conceptualization. **H. Baaziz:** Writing – review & editing, Software, Resources, Methodology, Formal analysis, Conceptualization.

Declaration of competing interest

The authors declare that they have no known competing financial interests or personal relationships that could have appeared to influence the work reported in this paper.

Data availability

Data will be made available on request.

References

[1] G. Springer, J.H.G. Laflamme, Can. Mineral. 10 (1971) 847.
[2] V.G. Kuznetsov, K.K. Palkina, A.A. Reshchikova, Inorg. Mater. 4 (1968) 585.
[3] E.I. Yarembash, E.S. Vigileva, Russ. J. Inorg. Chem. 7 (1962) 1435.
[4] V. Kramer, Thermochim. Acta 15 (1976) 205.
[5] B. Hamawandi, H. Mansouri, S. Ballikaya, Y. Demirci, M. Orlovská, N. Bolghanabadi, S.A. Sajjadi, M.S. Toprak, Front. Mater. 7 (2020) 569723.
[6] Elad Joseph, Yaron Amouyal, Towards a predictive route for selection of doping elements for the thermoelectric compound PbTe from first-principles, J. Appl. Phys. 117 (17) (2015) 175102, https://doi.org/10.1063/1.4919425.
[7] H. Kalpen, Diplomarbeit, University, Osnabruck, 1992.
[8] J. Chao, et al., Mater. Res. Bull. 98 (2018) 194–199.
[9] W. Huang, et al., Nanoscale 10 (2018) 2404–2412.
[10] H. Yu, et al., CrystEngComm 19 (2017) 727–733.
[11] A. Sarkar, et al., J. Colloid Interface Sci. 483 (2016) 49–59.
[12] X. Meng, Z. Zhang, J. Mol. Catal. A Chem. 423 (2016) 533–549.
[13] H. Abdullah, D.-H. Kuo, J. Phys. Chem. C 119 (2015) 13632–13641.
[14] J. Ni, et al., Adv. Energy Mater. 4 (2014) 1400798.
[15] G. Nie, X. Lu, J. Lei, L. Yang, C. Wang, Electrochim. Acta 154 (2015) 24–30.
[16] W. Yang, H. Wang, T. Liu, L. Gao, Mater. Lett. 167 (2016) 102–105.
[17] K. Biswas, L.D. Zhao, M.G. Kanatzidis, Adv. Energy Mater. 2 (2012) 634–638.
[18] Y. Cheng, et al., Angew. Chem. Int. Ed. 57 (2018) 246–251.
[19] Y. Yang, et al., Part. Syst. Charact. 32 (2015) 668–679.
[20] Z. Li, et al., RSC Adv. 7 (2017) 29672–29678.
[21] V. Kramer, Thermochim. Acta 86 (1985) 291.
[22] G. Chapuis, V. Ch Gnehm, Kramer, Acta Crystallogr. B 28 (1972) 3128 (9).
[23] H. Kalpen, W. Honle, M. Somer, U. Schwarz, K. Peters, H. Georg von Schnering, Z. Anorg, Allg. Chem. (1998) 624.
[24] K. Schwarz, P. Blaha, G.K.H. Madsen, Comput. Phys. Commun. 147 (2002). Aug.
[25] J.P. Perdew, Y. Wang, Phys. Rev. B 45 (1992) 13244–13249.
[26] A.D. Becke, E.R. Johnson, J. Chem. Phys. 124 (22) (2006) 221101.
[27] M. Jamal, M. Bilal, I. Ahmad, S. Jalali-Asadabadi, J. Alloys Compd. 735 (2018) 569–579.
[28] G.K.H. Madsen, D.J. Singh, Comput. Phys. Commun. 175 (2006) 67–71.
[29] A. Otero-de-la-Roza, V. Luaña, Comput. Phys. Commun. 182 (2011) 1708–1720.
[30] F.D. Murnaghan, Proc. Natl. Acad. Sci. USA 30 (9) (1944) 244–247.
[31] T. Ahmad Telfah, Z. Ghellab, H. Charifi, A.M. Alsaad Baaziz, Sahar Abdalla, R. F. Wai-Ning Mei, Sabirianov, Enhancing the thermoelectric performance of BiGa2X4 (X=S, se) P-type semiconductors by optimizing charge carrier concentration or chemical potentials, J. Phys. Chem. Solids 194 (2024) 112248, https://doi.org/10.1016/j.jpcs.2024.112248.
[32] T. Ghellab, H. Baaziz, Z. Charifi, M. Telfah, A. Alsaad, A. Telfah, R. Hergenröder, R. Sabirianov, The structural, electronic, optical, thermodynamical and thermoelectric properties of the Bi2Al4Se8 compound for solar photovoltaic semiconductors, Mater. Sci. Semicond. Process. 141 (2022) 106415, https://doi.org/10.1016/j.mssp.2021.106415.
[33] P.Y. Yu, M. Cardona, Springer, 2010.
[34] M. Fox, Oxford University Press, 2015.
[35] E. D. Palik (ed.), Academic Press, (1997).
[36] S. Lany, J. Phys. Chem. Lett. 2 (2011) 1223–1227.
[37] J. Tauc, Mater. Res. Bull. 3 (1968) 37–46.
[38] C.G. Van de Walle, J. Neugebauer, J. Appl. Phys. 95 (2004) 3851–3879.

[39] H.R. Philipp, J. Non-Cryst, Solids 8–10 (1972) 627–632.
[40] A. Tagrerout, H. Rached, M. Drief, Y. Guermit, S. Al-Qaisi, M. Caid, D. Rached, An extensive computational report on the quinary alloys Cu2Zn1−xCdxSnS4 for the solar cell systems: DFT simulation, Comp. Condensed Matter 31 (2022) e00670, https://doi.org/10.1016/j.cocom.2022.e00670.
[41] F. Zami, L. Djoudi, M. Merabet, S. Benalia, M. Boucharef, R. Belacel, D. Rached, The ground state, electronic and optical properties of the quaternary alloys BexCd1-xTeyS1-y /CdS for modeling quantum well lasers: ab-initio study within modified Becke-Johnson exchange potential, Optik 180 (2019) 873–883, https://doi.org/10.1016/j.ijleo.2018.11.068.
[42] N. Adim, M. Caid, D. Rached, O. Cheref, Computational study of structural, electronic, magnetic and optical properties of (ZnTe)m/(MnTe)n superlattices, J. Magn. Magn. Mater. 499 (2020) 166314, https://doi.org/10.1016/j.jmmm.2019.166314.
[43] F. Wooten, Academic Press, 1972.
[44] M. Dressel, G. Grüner, Cambridge University Press, 2002.
[45] M. Born, & K. Huang, Oxford University Press, (1954).
[46] J. F. Nye, Oxford University Press, (1985).
[47] F. Mouhat, F.X. Coudert, Phys. Rev. B 90 (22) (2014) 224104.
[48] R. Hill, Proceedings of the physical society, Sec. A 65 (5) (1952) 349.
[49] P. Ravindran, L. Fast, P.A. Korzhavyi, B. Johansson, J. Wills, O. Eriksson, J. Appl. Phys. 84 (9) (1998) 4891–4906.
[50] H.M. Ledbetter, A. Migliori, J. Appl. Phys. 100 (6) (2006) 063516.
[51] S.I. Ranganathan, M. Ostoja-Starzewski, Phys. Rev. Lett. 101 (5) (2008) 055504.
[52] A.G. Every, Phys. Rev. B 22 (4) (1980) 1746.
[53] R.F.S. Hearmon, Rep. Prog. Phys. 24 (1) (1961) 1.
[54] G.A. Slack, Solid State Phys. 34 (1979) 1.
[55] D.T. Morelli, V. Jovovic, J.P. Heremans, Phys. Rev. Lett. 101 (2008) 035901.
[56] Houssam Eddine Hailouf, K.O. Obodo, U. Hafid Aourag, P.K. Rani, K. Kamlesh, M. L. Verma Reggab, Souraya Goumri-Said, Deciphering dimensional transition effects in Bi2Se3 and Bi2Te3 topological insulators, Mater. Sci. Semicond. Process. 186 (2025) 109019, https://doi.org/10.1016/j.mssp.2024.109019.
[57] Mangal Chand Rolania, Peeyush Kumar Kamlesh, Pawan Kumar, Ghanshyam Sharma, Ajay Singh Verma, Insights into structural stability and thermal energy conversion into electrical properties of Mg3X2 (X = P, as, and Sb) compounds: a first-principles study, Mod. Phys. Lett. B (2024) 2550081, https://doi.org/10.1142/S0217984925500812.
[58] Rukaia Khatun, Atikur Rahman, Dayal Chandra Roy, Anjuman Ara Khatun, Mukter Hossain, Upasana Rani, Peeyush Kumar Kamlesh, Ahmad Irfan, Sarah Chaba Mouna, DFT study on the structural, mechanical, electronic, optical and thermodynamic properties of recently synthesized MAX phase compounds A3InC2 (a= Zr, hf) under ambient and elevated pressure, Materials Today Comm. 40 (2024) 109964, https://doi.org/10.1016/j.mtcomm.2024.109964.
[59] Ghanshyam Lal Menaria, Upasana Rani, Peeyush Kumar Kamlesh, Rashmi Singh, Monika Rani, Nihal Singh, Dinesh C. Sharma, Ajay Singh Verma, Electro-optic and transport properties with stability parameters of cubic KMgX (X = P, as, Sb, and bi) half-Heusler materials: appropriate for green energy applications, Mod. Phys. Lett. B 38 (2024) 2450283, https://doi.org/10.1142/S021798492450283X.
[60] S. Bougaa, H. Baaziz, T. Ghellab, S. Adalla, L. Bouhdjer, Ş. Uğur, G. Uğur, Z. Charifi, Mater. Sci. Semicond. Process. 188 (2025) 109185, https://doi.org/10.1016/j.mssp.2024.109185.
[61] T. Ahmad Telfah, Z. Ghellab, H. Charifi, A.M. Alsaad Baaziz, Sahar Abdalla, R. F. Wai-Ning Mei, Sabirianov, J. Phys. Chem. Solids 194 (2024) 112248, https://doi.org/10.1016/j.jpcs.2024.112248.
[62] B. Abdelkebir, F. Semari, Z. Charifi, H. Baaziz, T. Ghellab, Ş. Uğur, G. Uğur, R. Khenata, Phys. Scr. 99 (2024) 115924, https://doi.org/10.1088/1402-4896/ad7f99/meta.
[63] T. Ghellab, Z. Charifi, H. Baaziz, Solid State Commun. 389 (2024) 115594, https://doi.org/10.1016/j.ssc.2024.115594.
[64] Ghanshyam Lal Menaria, Upasana Rani, Peeyush Kumar Kamlesh, Monika Rani, Nihal Singh, Dinesh C. Sharma, Ajay Singh Verma, Comprehensive theoretical investigation of NaAlX (X=C, Si and Ge) half-Heusler compounds: unveiling the multifaceted properties for advanced applications, Int. J. Mod. Phys. B 39 (2024) 2550052, https://doi.org/10.1142/S0217979225500523.
[65] Naincy Pandit, Dubey, Anusha, Joshi, Tarun Kumar, Shukla, Akash, Rani, Upasana, Kamlesh, Peeyush Kumar, Gupta, Rajeev, Kumar, Tanuj, Kaur, Kulwinder, Verma, Ajay Singh, effect of anion (S−2 & se−2) replacement on photovoltaic properties in transition metal (Ba-barium) chalcogenide perovskites, Int. J. Mod. Phys. B 39 (2024) 2550059, https://doi.org/10.1142/S0217979225500596.